arXiv:1301.1655v2 [astro-ph.GA] 14 Jan 2013

Resolved Depletion Zones and Spatial Differentiation of N_2H^+ and N_2D^+[1]

John J. Tobin[2,3], Edwin A. Bergin[3], Lee Hartmann[3], Jeong-Eun Lee[4], Sébastien Maret[5], Phillip C. Myers[6], Leslie W. Looney[7], Hsin-Fang Chiang[7,8], Rachel Friesen[9]

ABSTRACT

We present a study on the spatial distribution of N_2D^+ and N_2H^+ in thirteen protostellar systems. Eight of thirteen objects observed with the IRAM 30m telescope show relative offsets between the peak N_2D^+ ($J = 2 \rightarrow 1$) and N_2H^+ ($J = 1 \rightarrow 0$) emission. We highlight the case of L1157 using interferometric observations from the Submillimeter Array and Plateau de Bure Interferometer of the N_2D^+ ($J = 3 \rightarrow 2$) and N_2H^+ ($J = 1 \rightarrow 0$) transitions respectively. Depletion of N_2D^+ in L1157 is clearly observed inside a radius of $\sim$2000 AU ($7''$) and the N_2H^+ emission is resolved into two peaks at radii of $\sim$1000 AU ($3.5''$), inside the depletion region of N_2D^+. Chemical models predict a depletion zone in N_2D^+ and N_2D^+ due to destruction of H_2D^+ at T $\sim$ 20 K and the evaporation of CO off dust grains at the same temperature. However, the abundance offsets of 1000 AU between the two species are not reproduced by chemical models, including a model that follows the infall of the protostellar envelope. The average abundance ratios of N_2D^+ to N_2H^+ have been shown to decrease as protostars

[1]Based on observations carried out with the IRAM 30m Telescope, the IRAM Plateau de Bure Interferometer, and the Submillimeter Array. IRAM is supported by INSU/CNRS (France), MPG (Germany) and IGN (Spain).

[2]Hubble Fellow, National Radio Astronomy Observatory, Charlottesville, VA 22903; jtobin@nrao.edu

[3]Department of Astronomy, University of Michigan, Ann Arbor, MI 48109

[4]Department of Astronomy and Space Science, Kyung Hee University, Yongin-si, Gyeonggi-do 446-701, Korea

[5]UJF-Grenoble 1 / CNRS-INSU, Institut de Planétologie et d'Astrophysique de Grenoble (IPAG) UMR 5274, Grenoble, F-38041, France

[6]Harvard-Smithsonian Center for Astrophysics, 60 Garden Street, Cambridge, MA 02138

[7]Department of Astronomy, University of Illinois, Urbana, IL 61801

[8]Institute for Astronomy, University of Hawaii at Manoa, Hilo, HI 96720

[9]National Radio Astronomy Observatory, Charlottesville, VA 22903

evolve by Emprechtinger et al., but this is the first time depletion zones of N_2D^+ have been spatially resolved. We suggest that the difference in depletion zone radii for N_2H^+ and N_2D^+ is caused by either the CO evaporation temperature being above 20 K or an H_2 ortho-to-para ratio gradient in the inner envelope.

1. Introduction

The dense (n $\sim 10^5$ cm^{-3}), cold (T$\sim$10 K) gas of starless or prestellar cores present one of the prime conditions for the formation of deuterated molecules in the interstellar medium. These conditions are needed to allow the formation of H_2D^+; reactions with this molecule and more highly deuterated isotopomers are the primary routes for molecules to gain molecular [D]/[H] ratios greater than the cosmic ratio of 10^{-5} within T $\sim$ 10 K gas (Watson 1974; Langer 1985). Furthermore, at these high densities and low temperatures, CO is frozen-out onto dust grains, increasing the rate of deuterium fractionation in the gas-phase, as CO is a primary destroyer of H_3^+ and H_2D^+ (e.g. Bergin & Tafalla 2007). A key molecular tracer of dense gas where CO has frozen out is N_2H^+ (e.g. Caselli et al. 2002). Its deuterated counterpart N_2D^+ is found to form with abundances relative to N_2H^+ of 5 - 10% in starless cores, with some extreme examples having 20 - 40% (Crapsi et al. 2005).

Shortly after the gravitational collapse of a starless core begins, a Class 0 protostar is formed within the dense core (Andre et al. 1993). This phase may last a few times 10^5 yr (Evans et al. 2009) and is accompanied by significant luminosity evolution and likely episodic accretion (Young & Evans 2005; Kenyon et al. 1990; Dunham et al. 2010). The combination of protostellar and accretion luminosity has a significant effect on the chemical abundances in the surrounding envelope (Lee et al. 2004). Regions near the protostar are heated above 20 K (R $\lesssim$ 1000 AU for low-mass/low-luminosity systems) and CO is evaporated off the dust grains back into the gas phase. Then as the protostellar luminosity increases with time, the region of CO evaporation increases as does the region where H_2D^+ is converted back into HD and H_3^+. Thus, cold deuterium chemistry is brought to a halt in the inner envelope (Roberts & Millar 2000; Caselli et al. 2008; Roberts & Millar 2007).

Emprechtinger et al. (2009) showed that this process of a growing CO evaporation and H_2D^+ destruction region will affect the N_2D^+ to N_2H^+ ratio and demonstrated how it could be used as an evolutionary indicator. The youngest Class 0 protostars are expected to have higher N_2D^+ to N_2H^+ ratios than more evolved Class 0 protostars. This is because the inside-out growth of the CO evaporation and H_2D^+ destruction region causes the overall abundance of N_2D^+ to drop relative to N_2H^+, due to the formation of N_2D^+ (and other deuterated species) being most efficient at the highest densities. Thus, as the luminosity

of the protostar increases with time, the N_2D^+ abundance will fall faster than the N_2H^+ abundance. The depletion zone of N_2D^+ may then be slightly larger (∼200 AU) than that of N_2H^+, shown by the chemical models in Emprechtinger et al. (2009).

Depletion zones of N_2H^+ have been spatially resolved previously, the most dramatic being IRAM 04191, with a 1600 AU radius N_2H^+ depletion zone (Belloche & André 2004). Other apparent depletion zones were pointed in Chen et al. (2007) and Tobin et al. (2011); depletion zones of NH_3 were also seen in some sources with N_2H^+ depletion regions (Tobin et al. 2011), as well as IRAM 04191 (Mangum et al. unpublished). However, most studies of deuterated molecules, in particular N_2D^+ (e.g. Roberts & Millar 2007), are primarily based on single-dish, single-point observations and do not spatially resolve or map the emission. N_2D^+ and N_2H^+ emission maps have been observed toward many starless cores and one protostellar core (Crapsi et al. 2004, 2005). These studies find close agreement between N_2H^+ and N_2D^+ distributions; however, a larger sample of N_2D^+ maps toward protostellar sources are lacking.

In conjunction with the N_2H^+ kinematics survey of Tobin et al. (2011), we simultaneously observed N_2D^+ toward a set of thirteen low-mass protostellar systems. Furthermore, we execute more detailed analysis of the protostellar system L1157 where we resolve symmetric depletion zones in both molecules using high-resolution interferometric observations. The symmetry and likely filamentary nature of the dense protostellar envelope around L1157 (e.g. Gueth et al. 2003; Looney et al. 2007; Tobin et al. 2010; Chiang et al. 2010) make it an ideal system for examining the detailed spatial distribution of these species. The observations and data analysis are described in Section 2, the observational results of the spatial distribution of N_2D^+ relative to N_2H^+ in L1157 and twelve other systems are described in Section 3, we compare a chemical model to L1157 in Section 4, the results are discussed and possible causes of the spatial offset of N_2D^+ relative to N_2H^+ are given in Section 5, and our main conclusions are given in Section 6.

2. Observations

This paper includes observations taken with the Submillimeter Array, the Plateau de Bure Interferometer and the IRAM 30m telescope. The properties of the selected sample are given in Table 1, with our sample being a subset of those in Tobin et al. (2011). We detail the observations and data reduction in the subsequent sections and list the relevant details of the observations in Tables 2 and 3.

2.1. SMA data

L1157 was observed with the Submillimeter Array (SMA) at Mauna Kea on 2009 September 15 in sub-compact configuration. The weather conditions were optimal with stable phases and less than 3 mm of precipitable water vapor, yielding a zenith opacity at 225 GHz of 0.1; system temperatures were between 120 and 150 K throughout the track. The receivers were tuned to the N_2D^+ ($J = 3 \rightarrow 2$) transition (ν=231.321635 GHz; Lovas (1992)) in the upper-sideband and 800 MHz of each side band was allocated to continuum; see Table 2 for a summary of observation details. The data were edited and calibrated using the MIRIAD software package (Sault et al. 1995); minimal flagging of uncalibrateable data was necessary (i.e. phase/amplitude jumps) and the T_{sys} correction was applied, putting the data on a Jansky amplitude scale. The nearby quasars 1849+670 and 1927+739 were used for phase and amplitude calibration, Mars was used for absolute flux calibration, and the quasar 3C454.3 was the bandpass calibrator. Uncertainty in absolute flux calibration is expected to be ∼10%.

2.2. IRAM 30m data

Observations were taken with the IRAM 30m radio telescope on Pico Veleta using the EMIR receiver over several nights during 2009 October (Table 3). For L1157, we observed the N_2D^+ ($J = 2 \rightarrow 1$) (ν=154.217096 GHz) and ($J = 3 \rightarrow 2$) (ν=231.321966 GHz) transitions along with the N_2H^+ ($J = 3 \rightarrow 2$) (ν=279.511701 GHz) and ($J = 1 \rightarrow 0$) (ν=93.173404 GHz) transitions, see Table 3 for details. We also observed 11 other sources in the N_2H^+ ($J = 1 \rightarrow 0$) and N_2D^+ ($J = 2 \rightarrow 1$) transitions simultaneously. System temperatures were between 100 K and 140 K at 93 GHz and between 110 K to 230 K at 154 GHz, see Table 3.

All data were taken in frequency-switched On-The-Fly (OTF) mapping mode. For L1157 in particular, the N_2D^+ ($J = 3 \rightarrow 2$) and N_2H^+ ($J = 3 \rightarrow 2$) lines were mapped in a $90'' \times 90''$ box centered on the protostar and N_2H^+ ($J = 1 \rightarrow 0$) and N_2D^+ ($J = 2 \rightarrow 1$) were observed in a $4' \times 3'$ box centered $30''$ south of the protostar. Data for the additional sources were generally observed in $3' \times 3'$ regions centered near the protostar. The OTF maps were constructed by fully scanning each source in both the north-south and east-west directions ($5''$ steps between scan legs); the orthogonal mapping directions minimize striping in the final map. The maps were repeated when necessary for a higher signal-to-noise ratio. We conducted system temperature measurements (calibration scans) about every 10 minutes and about 2 hours were needed to complete each map. The pointing offset was measured once every two hours, preceeding the observation of each source. The offsets were generally $\sim 5''$ and this offset was stable throughout an observing session, having variations of only

$\sim 2''$ from one pointing scan to the next. The RMS pointing accuracy of the telescope is $\sim 2''$ and our observed variations are consistent with this. The receiver offsets between the 3 mm and 2 mm bands were $\sim 2''$ and had been measured only a month before the data were taken; such a small offset will not affect our results.

The initial calibration of the OTF data to the antenna temperature scale and CLASS data format was performed automatically on-site by the Multichannel Imaging and calibration software for Receiver Arrays (MIRA)[2] package. The default amplitude calibration is expected to be accurate within $\sim$10%. Further data reduction was done using CLASS (part of GILDAS[2]). For all molecular lines observed, the frequency switched spectra were folded and baseline subtracted using a second order polynomial. We then reconstructed the spectral map on a grid such that the FWHM of the beam was spanned by 3 pixels and each pixel is the average of all measurements within the FWHM of the beam, see Tables 2 and 3, as well as Tobin et al. (2011) for additional details. Lastly, the emission maps were put on the T_{mb} scale where $T_{mb} = F_{eff}T_A^*/B_{eff}$. F_{eff} is the forward efficiency, accounting for losses by the secondary support structure, and B_{eff} is the main beam efficiency; values for F_{eff} and B_{eff} are dependent on frequency and given in Table 2.

2.3. PdBI data

L1157 was observed with the Plateau de Bure Interferometer in the N_2H^+ ($J = 1 \rightarrow 0$) transition in the D and C configurations in 2009 June and 2009 November. The data were edited, calibrated, and mapped using the CLIC and MAPPING components of the GILDAS software package. The absolute flux was derived from observations of MWC349, assuming a flux density of 1.15 Jy at 3 mm for that source; uncertainty in the absolute flux is $\sim$10%. More details on the data reduction are given in Tobin et al. (2011).

2.4. Single-Dish and Interferometric Combination

As an additional step, we combined the single-dish N_2H^+ data from the 30m with the PdBI data. We regridded the single-dish data to the phase center of the PdBI observations and resampled the velocity axis to correspond to the 0.125 km s^{-1} velocity resolution of the PdBI data. We did this using the MAPPING component of GILDAS, performing a joint deconvolution of the single-dish and interferometric data; GILDAS provides built-in

[2]http://www.iram.fr/IRAMFR/GILDAS

routines for combining the 30m data. The resulting image provides substantially better extended structure sensitivity than the default interferometric image shown in Tobin et al. (2011).

We also explored the possibility of combining the single-dish N_2D^+ data with the SMA N_2D^+ data for L1157. Unfortunately, the single-dish N_2D^+ ($J = 3 \rightarrow 2$) data had a lower signal-to-noise ratio than the SMA data, prohibiting a useful combination of the data.

2.5. Data Analysis and Hyperfine Fitting

The nuclear spin of nitrogen causes both N_2H^+ and N_2D^+ to have a hyperfine emission line spectrum. The multiple hyperfine components and line ratios of N_2H^+ (Caselli et al. 1995; Keto & Rybicki 2010) and N_2D^+ (Dore et al. 2004) enable us to simultaneously determine the line-center velocity, linewidth, optical depth, and excitation temperature at each point in the map.

CLASS was used to fit the hyperfine emission line structure, which can fit multiple lines given the optically thin line ratios and velocity offsets. The lines were fit at each pixel in the spectral map using a semi-automated routine. This routine used the integrated intensity map (zeroth moment) of the line emission, calculated from the total line intensity in a velocity range and multiplied by the channel velocity width. The pixels with at least a 3σ detection of N_2H^+ or N_2D^+ were selected and a CLASS script to fit the hyperfine line structure at each pixel was generated; the resultant fit parameters (line-center velocity, linewidth, optical depth, and excitation temperature) were written out to a text table. This criteria does not require 3σ detections of all line components and there were cases in which only the strongest hyperfine lines are detected. Bad fits resulting from inadequate signal-to-noise were removed to generate the final table of pixels with good fits. The typical failure mode of the fitting is excessively large linewidths (>1.5 km s^{-1}) and/or optical depths of 30, making the discrepant points easy to identify.

The integrated intensity, excitation temperature, and optical depths from line fitting are then used to calculate the column densities of the data following Goldsmith & Langer (1999). The column density maps generally trace regions where the integrated intensity was at least $\sim 6\sigma$ and usually 10σ. We use the excitation temperature of the N_2H^+ ($J = 1 \rightarrow 0$) in the calculation of N_2D^+ column density when the N_2D^+ ($J = 2 \rightarrow 1$) optical depth is less than 1.0. This is because the excitation temperature cannot be well-constrained if the lines are optically thin. If the excitation temperature of N_2D^+ ($J = 2 \rightarrow 1$) is actually lower than that of N_2H^+ ($J = 1 \rightarrow 0$), the N_2D^+ abundances would systematically underestimated. When

the N_2D^+ excitation temperatures could be constrained from the hyperfine fitting, they are comparable but generally lower than the values fit for N_2H^+ ($J = 1 \rightarrow 0$). The uncertainties in optical depth and excitation temperature lead to column density uncertainties of order $\sim$ 20% to 30%, in addition to a possible 10% amplitude calibration uncertainty. A few case have >100% uncertainty in the column densities due to large uncertainties in the optical depth.

We also computed spectra averaged within a 12″ radius (roughly the beamwidth at of the IRAM 30m at 93 GHz) centered on the position of each protostar. We used these spectra to derive average abundances and column densities toward the protostars for comparison with previous single-pointing studies (e.g. Roberts & Millar 2007; Emprechtinger et al. 2009).

3. Observational Results

We obtained simultaneous N_2D^+ and N_2H^+ mapping of twelve protostellar envelopes, as well as interferometric data in both species for L1157. The best example of spatially resolved N_2D^+ and N_2H^+ depletion is found toward L1157 in the interferometric data. We will discuss this source in detail first before presenting the rest of the sample.

3.1. L1157

The SMA continuum and N_2D^+ ($J = 3 \rightarrow 2$) data (4.3″×7.1″ resolution) for L1157 are shown in Figure 1, overlaid on the *Spitzer* IRAC 8 μm image. The 1.3 mm continuum data show that the source is strongly dominated by the point source emission coincident with the protostar, arising from the dense inner protostellar envelope. There is also extension along the outflow direction, likely due to warm gas associated with the inner outflow cavity. The outflow is nearly within the plane of the sky (Gueth et al. 1997) having an inclination of $\sim$85°. At lower intensity levels, the continuum emission is found to be extended along the dense envelope that was detected in extinction at 8 μm (Looney et al. 2007; Tobin et al. 2010) and in N_2H^+/NH_3 molecular line emission (Chiang et al. 2010; Tobin et al. 2011). This extension along the extinction lane was previously seen in the continuum with single-dish bolometer mapping at 850 μm and 1.3 mm (Gueth et al. 2003), but not in interferometric continuum data (Gueth et al. 1997, 2003; Chiang et al. 2010, 2012). The 3 mm continuum image from the PdBI is centrally peaked with no indication of extension along the envelope (Figure 1), consistent with Chiang et al. (2010). The detection of emission extended along the envelope with the SMA likely owes to the high-sensitivity of the observation, the short

uv-spacings in subcompact configuration, and the brighter dust continuum emission at 1.3 mm as compared to 3 mm.

The N_2D^+ ($J = 3 \rightarrow 2$) integrated intensity map (Figure 1), unlike the continuum data, is double-peaked, roughly symmetric about the protostar, with a local minimum coincident with the position of the protostar. The peaks are at radii of $\sim$ 2000 AU ($7''$) from the protostar and the emission closely correlates with opaque regions of the 8 μm extinction feature. In contrast, the N_2H^+ integrated intensity map from the PdBI+30m has emission peaks that are located at R$\sim$1000 AU ($3.3''$) from the protostar (Figure 1); the N_2D^+ emission peaks are 1000 AU further out. The double-peaked N_2H^+ emission appears at the same location in both the PdBI+30m image and the PdBI-only image from (Tobin et al. 2011). The symmetry about the protostar in N_2D^+ and N_2H^+ is striking, a strong indication that the protostar is affecting the abundance distribution of these molecules.

We also conducted single-dish mapping of N_2H^+ in the ($J = 3 \rightarrow 2$) and ($J = 1 \rightarrow 0$) transitions and N_2D^+ in the ($J = 3 \rightarrow 2$) and ($J = 2 \rightarrow 1$) transitions. The integrated intensity maps of these lines are shown in Figure 2 and spectra of all four lines toward the location of the protostar are shown in Figure 3. The N_2H^+ maps both appear centrally peaked and the ($J = 3 \rightarrow 2$) transition appears slightly elongated along the envelope axis, consistent with the resolved PdBI data. Both N_2D^+ maps show a double-peaked feature, coincident with the widely separated emission peaks observed in the SMA data.

The single-dish data having centrally peaked N_2H^+ ($J = 3 \rightarrow 2$) emission, double-peaked N_2D^+ ($J = 3 \rightarrow 2$) and ($J = 2 \rightarrow 1$) rule-out any excitation anomaly, optical depth, or interferometric filtering being responsible for the apparent central depletion of N_2D^+ emission around L1157. If the higher temperatures at smaller radii were causing the apparent central deficit of N_2D^+ ($J = 3 \rightarrow 2$), then the N_2H^+ ($J = 3 \rightarrow 2$) should have appeared to be similarly double-peaked. Optical depth is ruled out because fitting the hyperfine transitions of N_2D^+ finds them to be optically thin; the optically thin nature of the emission is apparent in the spectra shown in Figure 3 where the satellite lines emission lines are quite faint relative to the main lines. Therefore, we conclude that the deficit of N_2D^+ emission toward the protostar and the offset between interferometric N_2H^+ and N_2D^+ peaks reflects a reduction of N_2D^+ abundance relative to N_2H^+ in the inner envelope.

We used the interferometric N_2H^+ and N_2D^+ maps to construct column density maps of each species in order to construct a ratio map of N_2D^+ to N_2H^+. The N_2H^+ data have the single-dish data combined with the interferometer data to correct for missing flux. The N_2D^+ data have resolved out some flux, apparent from the negative contours in Figure 1; however, the total interferometric flux is comparable to the single-dish flux indicating that most emission is recovered in the SMA map. The SMA data were sampled with the same

pixel scale and phase center as the PdBI data and we calculated the column densities for each transition following Goldsmith & Langer (1999). The excitation temperature for N_2D^+ was taken from the hyperfine fits of N_2H^+ ($J = 1 \rightarrow 0$) at each point because the N_2D^+ ($J = 3 \rightarrow 2$) was optically thin and the excitation temperature could not be determined from hyperfine fitting. Figure 4 shows the SMA N_2D^+ ($J = 3 \rightarrow 2$) emission contours overlaid on the PdBI+30m N_2H^+ ($J = 1 \rightarrow 0$) map and shows the column density ratio of N_2D^+ relative to N_2H^+ in the adjacent panel. We then take one dimensional radial cuts of the column densities and ratio and plot them in Figure 5.

The line parameters for the average N_2H^+ and N_2D^+ spectra within a 12″ radius around the protostar are given in Table 4 and the column densities and ratios are given in Table 5. We calculate that L1157 has 3 times the level of N_2D^+ as measured by Emprechtinger et al. (2009), but a similar N_2H^+ column density. This may result from us having mapped the area surrounding the protostar, while Emprechtinger et al. (2009) appear to have only taken spectra in single pointings centered on the protostar. In which case, the 16″ beam at the frequency of N_2D^+ ($J = 2 \rightarrow 1$) would not have sampled the region of peak N_2D^+ emission with only one pointing. The single-dish ratio is also an order of magnitude higher than the minimum observed in the interferometer data, mainly due to the N_2H^+ column density being about and order of magnitude larger in the interferometer data. The lower column density in the single-dish data can be attributed to beam dilution and if we consider the column densities and ratios at 3600 AU radii (12″), then the interferometer data are consistent with the single-dish.

3.2. Other Sources

While we have given significant attention to L1157, observations of a larger sample show that N_2D^+ and N_2H^+ are often spatially differentiated and L1157 is not a special case. Figure 6 shows the N_2H^+ emission maps of the full sample overlaid on the IRAC 8 μm images, compared with the N_2D^+ emission maps. Figure 7 shows the column density maps of N_2H^+, N_2D^+, and the ratio of N_2D^+ to N_2H^+ for HH211 as an example and only the ratio maps are shown for the rest of the sample in Figure 8. The column densities are calculated by the method described in Section 2, using the integrated intensity corrected for optical depth and excitation temperature. The parameters of the N_2H^+ and N_2D^+ line fits are given in Table 4 and our column densities and ratios are given in Table 5. Our calculated column densities and ratios are consistent with those in Emprechtinger et al. (2009) within about a factor of two. The differences likely result from our exact centering on the protostar and our 12″ radius for averaging the spectra to derive an overall column density and abundance

ratio. The sources are briefly discussed individually below.

IRAS 03282+3035 – This source has a very dense envelope extended in the north-south direction, with nearly coincident N_2H^+ and N_2D^+ emission peaks. The ratio map indicates that the peak N_2D^+ abundance is offset from the protostar and N_2H^+ peak on one side only and to the south by 8″. This offset seems real and is larger than the 2″ receiver offset.

HH211 – This protostar was the most heavily deuterated object in Emprechtinger et al. (2009) and this is true of our sample as well (see Table 5), with a comparable ratio of N_2D^+ to N_2H^+. However, those measurements were toward the protostar position; the peak emission of N_2H^+ and N_2D^+ is offset to the southwest. Despite the N_2H^+ emission peak being offset from the protostar, the column density peak is centered on the protostar (Figure 7). The N_2D^+ column density peak is, however, offset southwest and the peak level of $N_2D^+/N_2H^+$is 0.28 at (-9″, 9″).

L1521F – This protostar was classified as a Very Low Luminosity Object (VeLLO) by Bourke et al. (2006) and was previously regarded as a starless core (Crapsi et al. 2004). The N_2D^+ emission peak may be slightly offset to the north relative to the N_2H^+; the overall spatial distribution of N_2D^+ appears quite flat; these maps are consistent with those of Crapsi et al. (2004). The column density ratio maps indicates that the N_2D^+ abundance may be reduced toward the central protostar.

IRAS 04325+2402 – This protostar is a multiple Class I source in Taurus, but with a large, dense core in close proximity, approximately located at (10, 25) in Figure 6 and offset from the protostar by ∼63″ (Scholz et al. 2010; Hogerheijde & Sandell 2000). The peak N_2H^+ emission is found to be north of the protostar, coincident with the nearby dense core seen in 8 μm extinction, with emission extending southward toward the protostars. The N_2D^+ emission is all located north of the protostar, coincident with the N_2H^+ peaks. The detection of N_2D^+ toward the protostar listed in Table 4 is marginal.

L1527 – L1527 is also in Taurus and Emprechtinger et al. (2009) did not detect N_2D^+ emission toward this source. However, we find that the N_2D^+ emission is concentrated north of the protostar by ∼70″ (10000 AU) and north of the N_2H^+ peak by ∼35″ (5000 AU), see Figure 6. Despite the large offset of N_2D^+ from the protostar, the submillimeter emission and 8 μm extinction are also more extended on the north-side of the protostar and coincide with the N_2D^+ emission (Tobin et al. 2010; Chandler & Richer 2000). Roberts & Millar (2007) also detected N_2D^+ toward this source in a lower resolution study with comparable column density. Despite the Class 0 status of L1527, it is very depleted in N_2D^+ relative to others in the sample. This could result from the wide outflow cavities increasing the overall

envelope temperature and driving down the deuteration.

RNO43 – This source was the most distant in the sample, associated with Orion. Nonetheless, we did find that the N_2D^+ emission was spatially offset from the N_2H^+ emission, with the N_2D^+ mostly on the west side of the protostar. The column density and ratio map is quite noisy due to the faintness of N_2D^+; moreover, the abundance of N_2D^+ relative to N_2H^+ may be overestimated due to beam dilution of the N_2H^+ map, given that RNO43 has the lowest N_2H^+ column density in the sample.

HH108 IRS – In the case of this protostar, the N_2D^+ and N_2H^+ emission are both centered to the southeast of the protostar. Unfortunately, the signal-to-noise of the N_2D^+ was too poor to make a useful column density ratio map.

HH108 MMS – This is the nearby neighbor of HH108 IRS, but is apparently less evolved and lower luminosity. Its ratio of N_2D^+ to N_2H^+ is about 4 times greater than HH108 IRS, consistent with the apparent youth of this protostar relative to HH108 IRS. The N_2D^+ emission from his protostar might be offset, but the noisy map makes this indefinite.

L483 – L483 is the strongest N_2H^+ source in the sample and most optically thick. The N_2D^+ emission peak is offset by $\sim 20''$ west of the protostar, with the highest N_2D^+ to N_2H^+ ratio at the location of peak N_2D^+ emission. However, the column density ratio map (Figure 8) indicates that there could be higher column density N_2D^+ coincident with the highest column density of N_2H^+.

L673 – The subregion of L673 mapped coincides with L673-SMM2 as identified by Visser et al. (2002), harboring a small clustering of young stars. The sources marked in Figure 6 and 8 correspond to the Class 0/I sources 13, 27, and 28 in Tsitali et al. (2010). The N_2D^+ emission is clearly not peaked at the same location as the N_2H^+ emission and the column density is substantially reduced. The average N_2H^+ to N_2D^+ ratios are fairly constant and low for the three identified sources. However, the northern most source (28) may be at the location of higher N_2D^+ abundance as shown in the column density and ratio maps, but this is uncertain.

L1152 – L1152 is comprised of two cores seen in N_2D^+ and N_2H^+ emission linked by an apparent filament of material. The protostellar core in the south has strong N_2D^+ and N_2H^+ emission, but offset from the protostar. The peak N_2D^+ to N_2H^+ ratios in the south (protostellar) and north (starless) are 0.09 and 0.11 respectively.

L1157 – We performed the same analysis on L1157 as the rest of the sample for completeness, the drop in N_2D^+ abundance is not apparent in the single-dish ratio map (Figure 8), but there is a slight depression of emission in the N_2D^+ ($J = 2 \rightarrow 1$) map. The aver-

age N_2D^+ to N_2H^+ ratio of 0.12 is consistent with averaging the minimum and maximum abundance ratio from the interferometer data.

L1165 – Similar to L483, the N_2D^+ emission is also shifted along the outflow in L1165. The emission does seem to extend back toward the N_2H^+ peak that is southeast of the protostar. The small area of N_2D^+ emission makes a ratio map uninteresting, but the source has one of the lowest ratios of N_2D^+ to N_2H^+ from the single-point analysis; however this could be affected by beam dilution.

Including L1157, eight of the thirteen sources show spatial shifts in the peak emission or column density of N_2D^+ relative to N_2H^+. Although L673 is included, it could be argued that it is different since its environment is more complex due to having several young stars within a 0.1 pc diameter region. It is also important to note that we are limited by resolution in many cases, so some sources could have shifts that are not detectable in the 30m data. The N_2H^+ and N_2D^+ shifts can be regarded with high confidence because the data were taken simultaneously and the receivers are aligned to within $2''$ accuracy. The relative offset between N_2H^+ and N_2D^+ peaks are tabulated in Table 5. In addition to N_2D^+ being shifted relative to N_2H^+, there are also offsets between the peak emission of N_2H^+ and the protostars in six of the thirteen sources (HH108 IRS, L1152, L1165, HH211, L1527, and IRAS 04325+2402).

While spatial differentiation between the species is quite prevalent, the location of the peaks relative to the protostar is often not as well-ordered as L1157. We observe a trend in the sample in which the apparently youngest sources, as classified from their cold bolometric temperatures (T_{bol}) (Table 1) (HH211, HH108MMS, IRAS 03282+3035, and L1521F) do not show as strong spatial differentiation between N_2D^+ and N_2H^+. The more evolved protostars (with warmer T_{bol} and wide outflows (Arce & Sargent 2006)) have the largest spatial offset between N_2D^+ and N_2H^+ (L1527 and IRAS 04325+2402).

We also compare the N_2D^+ to N_2H^+ ratios to the bolometric luminosity and temperature in Figure 9. There is not a clear trend in bolometric luminosity, only that more luminous sources tend to have less deuteration while lower luminosity sources may be more highly deuterated or not. There does appear to be a trend of decreasing N_2D^+ to N_2H^+ ratio with increasing bolometric temperature, indicating that the deuteration may be decreasing with protostellar evolution. However, there is significant scatter at low bolometric temperatures.

3.3. Kinematics of N_2D^+ versus N_2H^+

The difference in relative spatial distributions between N_2D^+ and N_2H^+ in most systems is an indication that these molecules are not tracing the same material throughout the envelope. This suggests that the kinematic structure probed by these tracers is likely different. We compare the kinematics of the two tracers for L1157 in Figures 10 & 11, using both single-dish and interferometric kinematics respectively. For L1157, we notice a similar large-scale velocity gradient in both N_2H^+ and N_2D^+; however, near the protostar, where the N_2D^+ abundance drops, there are clear differences. The line-of-sight velocities measured from N_2D^+ on the west side of the envelope appear systematically larger by about 0.1 km s^{-1} as compared to the N_2H^+ data; this is present in both the single-dish and interferometric data. This region is located near the blueshifted outflow cavity and could be due to N_2H^+ being entrained by the outflow (Tobin et al. 2011), skewing the line profile toward blue-shifted velocities. Since the N_2D^+ abundance is peaked at larger radii, it may not be affected by the outflow as strongly as N_2H^+. Thus, the N_2D^+ could be tracing an increased velocity gradient due to rotation and/or infall (Tobin et al. 2011, 2012) that is masked by the outflow interaction with N_2H^+.

The linewidth of N_2H^+ is also found to be larger than N_2D^+ within $10''$ of the protostar in both the single-dish and interferometer data. Thus, the signature of the outflow-envelope interaction is not as pronounced in N_2D^+ due to its lower abundance on scales less than 2000 AU. This is a clear indication that on small-scales, the N_2D^+ is not tracing the same gas as N_2H^+. Moreover, this demonstrates that N_2H^+ is able to probe closer to the protostar and disk forming region of the envelope during this stage of evolution.

4. Chemical Model Comparison

L1157 represents an ideal case to test chemical models for a protostellar source due to the higher resolution data, excellent signal-to-noise, and well-known orientation in the plane of the sky. Moreover, the relative symmetry of the filamentary envelope (Tobin et al. 2010), N_2H^+, and N_2D^+ emission on scales less than 5000 AU make chemical modeling of this source more tractable. We will first review the critical chemical processes at work, affecting the formation and abundance of N_2H^+ and N_2D^+.

4.1. Relevant Chemical Processes

Deuterium chemistry in the cold (T$\sim$ 10 K) interstellar medium begins with the formation of H_2D^+, dominated by the reaction

$$H_3^+ + HD \rightleftharpoons H_2D^+ + H_2 + \Delta E \tag{1}$$

where $\Delta E \sim 230$ K (Herbst 1982). At low temperatures (T $\lesssim$ 20 K) the forward reaction will dominate causing H_2D^+ to have an abundance approaching that of H_3^+ in cold, dense cores (Langer 1985). The high abundance of reactive H_2D^+ enables subsequent deuterated molecules further down the reaction chain to have abundances elevated above the cosmic [D/H] $\sim 10^{-5}$, including D_2H^+ and D_3^+ (Caselli et al. 2008; Pagani et al. 2009). The abundance of H_2D^+ is limited by recombination with electrons and reactions with other molecules. The back reaction can also become non-negligible at T $\sim$ 20 K, leading to decreased deuteration even before CO has been liberated from the dust (Emprechtinger et al. 2009).

At T $<$ 20 K, most CO is frozen-out onto dust grains at the densities of protostellar cores (n$\sim 10^5$ cm^{-3}), but once the protostar raises the temperature to $\gtrsim$ 20 K, the CO ice sublimates back to the gas phase. When CO is in the gas phase, all the available carbon not locked into dust grains will react, effectively shutting off the deuterium chemistry as initiated by H_2D^+; an additional route to deuterium fractionation is available through CH_2D^+at T $>$ 30 K, but this does not cause subsequent N_2D^+ formation. Furthermore, the H_2 ortho-to-para ratio of the cloud can affect the overall deuterium fractionation; ortho-H_2 is in the J=1 state with an energy above the ground of 170 K. This has enough energy to lower the potential barrier of the back reaction of Equation 1 even at low temperatures, making the overall level of deuteration sensitive to the H_2 ortho-to-para ratio (Flower et al. 2006; Pagani et al. 2009).

The primary formation route for N_2H^+ is the gas phase reaction

$$N_2 + H_3^+ \rightarrow N_2H^+ \tag{2}$$

and N_2D^+ is understood to form via the same process, but with H_2D^+ as the reactant. Thus, the ability to form N_2D^+ is constrained by the conditions in which H_2D^+ exists. Both N_2D^+ and N_2H^+ are destroyed by reactions with CO, therefore, they are only expected to be present with significant abundance in regions where CO has depleted. In low-mass/luminosity protostellar systems, the temperatures only rise above 20 K at radii less than 1000 AU. Thus, the results from chemical modeling lead us to expect N_2D^+ and N_2H^+ to trace the same gas where CO is frozen-out onto dust grains (e.g. Emprechtinger et al. 2009; Pagani et al. 2009).

4.2. Chemical Model

We compare our data with the evolutionary chemical model of Lee et al. (2004). Since L1157 has formed a protostar, a model that accounts for the infalling material as well as the evolution of radiative heating is important. This model endeavors to simulate the chemistry of an isolated protostellar cloud through the prestellar phase as approximated by a Bonnor-Ebert sphere and then transition to the protostellar phase using the inside-out collapse model (Shu 1977) with an initially isothermal temperature of 10 K. The protostellar phase includes luminosity evolution following the prescription of (Young & Evans 2005) with radiative transfer calculated by DUSTY, but not including episodic accretion bursts. The chemistry of the infalling gas parcels is calculated discretely and the inward radial motion is tracked within the model.

Since the chemical model calculates a 1D radial abundance profile, we took several steps to make a more realistic observational comparison. We used the input radial density profile from the chemical model and the calculated abundance profile to construct a circular envelope midplane. We then summed the density along the line of sight through the envelope to calculate the predicted column density distribution in order to compare with the observations. Since L1157 is likely a filament rather than a sheet (Tobin et al. 2010), we also tapered the circular sheet by a Gaussian along the assumed line of sight with scale height parameters of 500, 750, 1000, and 2000 AU in order to simulate a filamentary density distribution. However, we note that the chemical abundances calculated for a 1D density profile will not exactly map to a filamentary envelope, but should be a reasonable approximation. Our goal was not to fit L1157 in detail with the model, but to look for a general agreement with the observed radial distribution and abundance ratio of the two species.

In Figure 12, we show a plot of the N_2D^+ to N_2H^+ column density ratios as a function of radius from the model. We clearly see the drop in abundance of the two species at radii less than 1000 AU due to reactions with CO and their abundances peak at intermediate radii between 1000 and 5000 AU, with decreasing abundances at larger radii. The model that best fits the abundance ratio of L1157 has evolved for 300,000 yr after collapse and the luminosity of the model (5 $L_\odot$) is comparable to what is observed. While the abundance ratio of N_2D^+ relative to N_2H^+ matches the data reasonably well, the column density and abundance peaks of N_2H^+ and N_2D^+ are nearly coincident with each other, inconsistent with the data shown in Figure 12. Earlier and later timesteps of the model also show coincident peaks between these two molecules. Thus, predicted ratio of N_2D^+ and N_2H^+ is consistent with the model, but the absolute abundances/column densities are inconsistent.

It is important to point out that the column density peak of N_2D^+ is in agreement with the observed N_2D^+ column density peak and the N_2H^+ column density peak of the

model is what disagrees with the observations. The inability of the model to reproduce the abundance peak offsets between the N_2D^+ and N_2H^+ may indicate that the models may not be capturing some physical process; we will discuss this further in the following section.

5. Discussion

It has been previously shown that the depletion of N_2D^+ relative to N_2H^+ is expected in protostars (Roberts & Millar 2007; Emprechtinger et al. 2009), but the ∼1000 AU spatial differentiation between the peaks of the two species is not matched by our chemical modeling, nor that of Emprechtinger et al. (2009). Moreover, the only other study to recognize the spatial offset of N_2H^+ and N_2D^+ was Friesen et al. (2010) with observations of the protocluster Oph B2. However, such spatial offsets have not been observed toward individual/isolated protostellar systems previously. Spatially resolved observations of deuterated molecules relative to their normal counterparts offer crucial tests to chemical models and further our understanding of the evolution of deuterated molecules in protostellar systems.

5.1. N_2H^+ Depletion Zones

As pointed out in the introduction, a N_2H^+ depletion zone had been observed previously toward the Class 0 protostar IRAM 04191 (Belloche & André 2004). This source is recognized as a Very Low Luminosity Object or VeLLO, having an internal luminosity of < 0.1 $L_\odot$. The depletion zone in IRAM 04191 has a radius of 1600 AU, larger than that of L1157 and other protostars observed by Chen et al. (2007) and Tobin et al. (2011). However, the disappearance of N_2H^+ could be explained by either freeze-out onto dust grains, as apparently observed in the pre-stellar core B68 (Bergin et al. 2002), or the destruction of N_2H^+ due to CO being released from dust grains as a result of protostellar heating (e.g. Lee et al. 2004). Such a large depletion zone in IRAM 04191 produced via N_2H^+ destruction from evaporated CO would not work given the low system luminosity and Belloche & André (2004) suggested freeze-out of N_2 onto dust grains as the likely mechanism for N_2H^+ depletion. Alternatively, Lee (2007) constructed an episodic accretion model that could also explain the size of the depletion zone with a recent burst of luminosity in IRAM 04191. L1157 and the other protostars known to have resolved N_2H^+ depletion zones are of order 5 to 10 $L_\odot$. These protostars could evaporate CO from dust grains out to sufficiently large radii with equilibrium heating to explain the size of the depletion zones.

5.2. Cause of N_2H^+ and N_2D^+ Emission Offsets

The inability of the chemical model used here (Lee et al. 2004) and others in the literature (Emprechtinger et al. 2009) to reproduce the relative offset of the column density peaks for both species is troubling at first. However, this may not mean that our understanding of the chemical processes forming and destroying the molecules is wrong. The presence of the central protostar, raising the gas and dust temperatures above ∼10 K introduces significant complexities to the chemistry within ∼2000 AU of the protostar, as compared to the prestellar phase. Moreover, since we are considering the radial abundances of two molecules, we must determine whether it is the N_2D^+ or N_2H^+ that is problematic.

As outlined in the previous section, the reaction that forms H_2D^+, leading to the formation of N_2D^+, is only active at temperatures less than 20 K; at greater temperatures the H_2D^+ reacts with H_2 and is converted back to H_3^+ and HD (Equation 1). Furthermore, T $\sim$ 20 K is also the temperature at which CO is evaporated off of dust grains and can freely react with and destroy N_2D^+ and N_2H^+. A $C^{18}O$ map of L1157 detects an emission peak at the protostar and very little CO at radii larger than 1200 AU (Jørgensen et al. 2007), consistent with the location of the N_2H^+ abundance peaks. CO will destroy N_2D^+ as quickly as it destroys N_2H^+, so reactions with CO will affect the abundance distribution of both molecules in the same manner. In order to have an abundance peak of N_2H^+ inside that of N_2D^+, one needs to have a range of radii where the H_2D^+ abundance is reduced and CO is not significantly present in the gas phase. Figure 13 shows a schematic diagram of the spatial zones in L1157 where N_2H^+, N_2D^+, and the two molecules governing the spatial distribution of emission are located (CO and H_2D^+). Of these molecules, only observations of H_2D^+ are lacking.

The relevant processes in the protostellar envelope that could affect the spatial distribution of molecules are protostellar heating, outflows, and infall. Emprechtinger et al. (2009) presented chemical models that considered protostellar heating and the H_2D^+ abundances becoming reduced at radii somewhat larger than CO sublimation; however, the shifts of N_2D^+ peak abundances were only ∼200 AU outside of the N_2H^+ peak and unable to explain the 1000 AU offset in L1157. Replenishment of N_2H^+ and N_2D^+ via infall from the outer envelope is built into Lee et al. (2004) model, but N_2H^+ and N_2D^+ remain coincident at all time steps. Tobin et al. (2011) showed that the protostellar outflow is entraining N_2H^+ at the 1000 AU scale; however, such entrainment would affect N_2D^+ in the same way that it affects N_2H^+. Moreover, N_2D^+ does not appear to be significantly affected by the outflow as evidenced by its narrower linewidth than N_2H^+ (Figure 10).

Another possibility considered was episodic accretion (e.g. Kenyon et al. 1990; Dunham et al. 2010). If there was an accretion outburst, it could temporarily heat the envelope to

T $\gtrsim$ 20 K out to ∼2000 AU. Then all the H_2D^+ could have been converted back to H_3^+ and HD. Moreover, CO would be liberated from the dust grains destroying the N_2H^+ and N_2D^+ present (Lee 2007; Visser & Bergin 2012). After the luminosity decreases and CO freezes back out, N_2H^+ would be able to form directly, while N_2D^+ would have to wait until H_2D^+ has reformed. Thus, we considered the possibility that N_2H^+ could reform faster than N_2D^+ since it is a one-step process and N_2D^+ takes two steps to form. While this scenario is attractive, work by Lee (2007); Visser & Bergin (2012) shows that the chemistry is governed by the CO freeze-out timescale after an accretion outburst and N_2D^+ and N_2H^+ should reform in lockstep. Thus, episodic accretion alone cannot adequately account for the observed spatial distribution of N_2H^+ and N_2D^+.

An additional scenario we considered is an H_2 ortho-to-para (OPR) gradient in the envelope. The steady-state OPR in cold (T ∼ 10 K) clouds is calculated to be $\sim 2.7\times10^{-3}$ Flower et al. (2006), whereas H_2 forms with OPR = 3 from statistical equilibrium. OPR values larger than steady-state would decrease the deuteration by enabling the back reaction of H_2D^+ formation to be active (Equation 1). Since the protostar likely went through a cold starless phase with a duration of 10^4 to 10^6 yr the H_2 OPR throughout the cloud was likely around the equilibrium value before collapse (Parise et al. 2011). Once the protostar forms and begins to heat the inner envelope, the OPR ratio could increase; Sipilä et al. (2010) shows a sharp increase at T > 15 K. Such an OPR ratio gradient going into the warm inner envelope could explain the large region of N_2D^+ depletion. However, it is unclear if this could reproduce the observations given that the OPR is still quite low ($\sim 10^{-4}$). There is also a question of timescales given that the steady-state timescale in Sipilä et al. (2010) is $\sim 10^5$ yr, longer than the infall timescale for material to fall in from 2000 AU to 1000 AU ($\sim 10^4$ yr assuming a 0.5 $M_\odot$ protostar). While there are some problems with this scenario, it cannot be ruled out.

A final scenario to produce the observed abundance offsets is a CO evaporation temperature is higher than 20 K. The temperatures for H_2D^+ destruction and CO evaporation are quite close and if the CO evaporation temperature was even just a few degrees higher than 20 K, this could be enough to explain the observed emission offsets, as was true in the Emprechtinger et al. (2009) models. We illustrate this in Figure 13, where if the CO remained mostly frozen-out between 20 to 25 K, this could explain the emission offsets by enabling N_2H^+ to be present in this warmer region at smaller radii than N_2D^+. It is possible that the CO evaporation temperature could vary since the physical state of CO ice can be much more complex. The CO may be mixed with other ices: NH_3, CO_2,CH_3OH, H_2O, etc. The binding energy of CO to other ices tends to be strong than CO to CO (Collings et al. 2004; Fayolle et al. 2011), therefore ice mixtures having slightly larger evaporation temperatures could explain the observations. However, it is uncertain how mixed the ice is because some species

tend to freeze-out more quickly, forming ice layers rather than a single mixed layer (Öberg et al. 2011). Aside from the caveat of unknown ice mixtures, a slightly altered evaporation temperature of CO ice due to mixing would explain our observations quite simply without needing episodic accretion and/or H_2 OPR gradients. But, episodic accretion could cause more ice mixing and conversion of CO ice to CO_2 may build an ice mixture with a large enough binding energy to remain frozen at T > 20 K (Kim et al. 2012).

In summary, the abundance peak offsets between N_2D^+ and N_2H^+ could be explained by either an H_2 OPR gradient in the inner envelope or an increased CO evaporation temperature due to ice mixtures. The chemical model of Lee et al. (2004) does not calculate a temperature dependent H_2 OPR, which may explain why it does not reproduce the abundance peak offset between N_2D^+ and N_2H^+. At the same time, the model also does not allow for ice mixtures to increase the evaporation temperature CO, which could cause the N_2H^+ peak to move inward. However, the chemical model does have its N_2D^+ column density/abundance peak at roughly the same radius as the observations, this offers some evidence for the increased CO evaporation temperature scenario, i.e. the deuterium chemistry produced the expected results for N_2D^+ but N_2H^+ is divergent. Though, we cannot conclusively distinguish between these two scenarios as both seem likely to occur and could be simultaneously contributing to make the shift in abundance peaks stronger.

5.3. Envelope and N_2D^+/N_2D^+ Emission Morphology

An additional effect to consider is the viewing angle and three dimensional envelope density structure in relation to the observed N_2D^+ emission morphology. In the case of L1157, there is evidence that the envelope is filamentary rather than sheet-like (Tobin et al. 2010). A filamentary envelope can have two effects on the apparent N_2H^+ and N_2D^+ depletion zones. First, the depletion zones are likely more apparent in a filamentary geometry than in a axisymmetric sheet, due to less emission superimposed along the line of sight in than an axisymmetric object; this is demonstrated in the column density plots in Figure 12. Also, the orientation of a filament within the plane of the sky can change the apparent size of the depletion regions; however, viewing angle effects would only make the depletion regions smaller and not larger. Thus, no complicated viewing angle effects could give the illusion of large N_2D^+ depletion zones outside those of N_2H^+. In the case of L1157, we cannot attribute the observed morphology to observational bias due to the symmetry of the depletion zones and abundance peaks.

The rest of the sample is not as well-ordered as L1157 in terms of envelope structure and/or emission morphology. L1527, L1165, L1152, HH108 IRS, HH211, and IRAS

04325+2402 have N_2H^+ emission peaks that are not coincident with the protostar, but the N_2D^+ emission is never peaked closer to the protostar that N_2H^+. L483 and L1165 show N_2D^+ emission peaked in the direction of the outflow rather than perpendicular to it. In these cases of complex emission morphology, the heating of the protostar and the envelope structure are both contributing to the complex emission morphology. L483 shows N_2H^+, NH_3, and 850 μm emission that are oriented at a 45° angle to the outflow direction (Fuller & Wootten 2000; Shirley et al. 2000), roughly the same direction as the N_2D^+ emission. Therefore, the N_2D^+ emission apparently extended along the outflow is simply shifted in the direction of the high-density envelope structure and the highest density material is simply not perpendicular to the outflow.

Moreover, the envelopes with less complex structure near the protostar in 8 μm extinction and N_2H^+ (i.e. L1521F, IRAS 03282+3035, HH211, and L1157) do not have irregular N_2D^+ distributions. These sources, except for L1157, appear to have N_2D^+ emission peaks possibly shifted to one side of the envelope. Thus, we can conclude that if the envelope has highly irregular structure, then we expect this to create an irregular distribution of N_2D^+. Furthermore, the frequent offsets of N_2D^+ emission from the protostars, even though it may be coincident with the N_2H^+ peak, means that N_2D^+ is not tracing the densest material in protostellar cores. Thus, caution must be exercised when interpreting the kinematics of the deuterated species without observations of both as deuterated species cannot be relied upon to trace the densest and/or same material as non-deuterated in the presence of temperature gradients.

5.4. Chemical Evolution

It is important to stress that even though N_2D^+ and N_2H^+ are not always spatially coincident as previously assumed and indicated by chemical models, our results do not disagree with the generalized picture of chemical evolution in protostellar cores (e.g. Lee et al. 2004; Roberts & Millar 2007; Emprechtinger et al. 2009). Specifically, the reduced abundance of N_2D^+ relative to N_2H^+ as protostar evolve is consistent with our data as shown in Figure 9 and the previous work; moreover, the spatial offsets of N_2D^+ relative to N_2H^+ appear to be a product of this chemical evolution and contribute to the relative decrease of N_2D^+ relative to N_2H^+. Given the two scenarios we outline for the cause of the peak offsets, further chemical modeling that accounts for infall, H_2 OPR gradients, and changes in the CO evaporation temperature is needed to fully understand the exact cause. Sensitive, spatially-resolved observations of both $C^{18}O$ and H_2D^+ could determine if the increased evaporation temperature is likely, as we would expect to see a gap between the

two species if this were the case.

6. Summary and Conclusions

We have presented a detailed study of the relative spatial distribution of N_2D^+ and N_2H^+ in Class 0/I protostellar envelopes from interferometric observations of L1157 and single-dish data of thirteen sources (L1157 included). We find that N_2H^+ and N_2D^+ often do not have the same column density distribution, given that the emission peaks of the two species are not spatially coincident, contrary to predictions by previous chemical models.

1. The depletion regions of both N_2H^+ ($J = 1 \rightarrow 0$) and N_2D^+ ($J = 3 \rightarrow 2$) in the envelope around the Class 0 protostar L1157 are well-resolved in interferometric observations with the PdBI and SMA respectively. Both N_2D^+ and N_2H^+ are double-peaked with the N_2D^+ peaks at R$\sim$2000 AU, outside the peaks of N_2H^+ which are at R$\sim$1000 AU. Follow-up single-dish observations from the IRAM 30m of N_2H^+ ($J = 3 \rightarrow 2$), N_2D^+ ($J = 3 \rightarrow 2$), and ($J = 2 \rightarrow 1$) confirm the spatial offsets of the species.

2. Subsequent observations of additional protostellar envelopes in N_2H^+ ($J = 1 \rightarrow 0$) and N_2D^+ ($J = 2 \rightarrow 1$) with the IRAM 30m show frequent offsets between the emission peaks of N_2D^+ and N_2H^+ in eight of thirteen sources (L1157 included). Some sources without offsets could be due to a lack of spatial resolution; moreover, the additional sources with spatial offsets are not as well-ordered as L1157.

3. The large ($\sim$1000 AU) offset in abundance peaks of N_2H^+ and N_2D^+ is not matched by the dynamic chemical model, nor previously published static models from (Emprechtinger et al. 2009). In such models, the abundance ratio of N_2D^+ and N_2H^+ falls due to heating by the protostar, but the abundance peaks remain closely coincident.

4. We suggest that the emission offsets are best explained by either an increased CO evaporation temperature due to ice mixtures or an H_2 ortho-to-para ratio gradient. In the case of an increased CO evaporation temperature, there would be a region where H_2D^+ is not present in the gas phase, but CO is still frozen-out, enabling N_2H^+ have its emission peak be inside of the N_2D^+ peak. However, an H_2 ortho-to-para ratio gradient would appear observationally similar and both effects may be happening.

We thank the referee Paola Caselli for helpful comments that improved the final manuscript. The authors wish to acknowledge useful discussions with K. Oberg. We thank the SMA staff for carrying out the observations, IRAM 30m staff for allowing us to use the E330 receiver with its interim local oscillator in the Fall of 2009 and assistance with the observations.

The Submillimeter Array is a joint project between the Smithsonian Astrophysical Observatory and the Academia Sinica Institute of Astronomy and Astrophysics and is funded by the Smithsonian Institution and the Academia Sinica. J.Tobin acknowledges support provided by NASA through Hubble Fellowship grant #HST-HF-51300.01-A awarded by the Space Telescope Science Institute, which is operated by the Association of Universities for Research in Astronomy, Inc., for NASA, under contract NAS 5-26555. The National Radio Astronomy Observatory is a facility of the National Science Foundation operated under cooperative agreement by Associated Universities, Inc.

REFERENCES

Andre, P., Ward-Thompson, D., & Barsony, M. 1993, ApJ, 406, 122

Arce, H. G., & Sargent, A. I. 2006, ApJ, 646, 1070

Belloche, A., & André, P. 2004, A&A, 419, L35

Bence, S. J., Richer, J. S., & Padman, R. 1996, MNRAS, 279, 866

Bergin, E. A., Alves, J., Huard, T., & Lada, C. J. 2002, ApJ, 570, L101

Bergin, E. A., & Tafalla, M. 2007, ARA&A, 45, 339

Bourke, T. L., Myers, P. C., Evans, II, N. J., Dunham, M. M., Kauffmann, J., Shirley, Y. L., Crapsi, A., Young, C. H., Huard, T. L., Brooke, T. Y., Chapman, N., Cieza, L., Lee, C. W., Teuben, P., & Wahhaj, Z. 2006, ApJ, 649, L37

Caselli, P., Benson, P. J., Myers, P. C., & Tafalla, M. 2002, ApJ, 572, 238

Caselli, P., Myers, P. C., & Thaddeus, P. 1995, ApJ, 455, L77

Caselli, P., Vastel, C., Ceccarelli, C., van der Tak, F. F. S., Crapsi, A., & Bacmann, A. 2008, A&A, 492, 703

Chandler, C. J., & Richer, J. S. 2000, ApJ, 530, 851

Chapman, N. L., & Mundy, L. G. 2009, ApJ, 699, 1866

Chen, X., Launhardt, R., & Henning, T. 2007, ApJ, 669, 1058

Chiang, H., Looney, L. W., & Tobin, J. J. 2012, ApJ submitted

Chiang, H., Looney, L. W., Tobin, J. J., & Hartmann, L. 2010, ApJ, 709, 470

Chini, R., Ward-Thompson, D., Kirk, J. M., Nielbock, M., Reipurth, B., & Sievers, A. 2001, A&A, 369, 155

Collings, M. P., Anderson, M. A., Chen, R., Dever, J. W., Viti, S., Williams, D. A., & McCoustra, M. R. S. 2004, MNRAS, 354, 1133

Crapsi, A., Caselli, P., Walmsley, C. M., Myers, P. C., Tafalla, M., Lee, C. W., & Bourke, T. L. 2005, ApJ, 619, 379

Crapsi, A., Caselli, P., Walmsley, C. M., Tafalla, M., Lee, C. W., Bourke, T. L., & Myers, P. C. 2004, A&A, 420, 957

Dore, L., Caselli, P., Beninati, S., Bourke, T., Myers, P. C., & Cazzoli, G. 2004, A&A, 413, 1177

Dunham, M. M., Evans, N. J., Terebey, S., Dullemond, C. P., & Young, C. H. 2010, ApJ, 710, 470

Emprechtinger, M., Caselli, P., Volgenau, N. H., Stutzki, J., & Wiedner, M. C. 2009, A&A, 493, 89

Enoch, M. L., Evans, N. J., Sargent, A. I., & Glenn, J. 2009, ApJ, 692, 973

Enoch, M. L., Glenn, J., Evans, II, N. J., Sargent, A. I., Young, K. E., & Huard, T. L. 2007, ApJ, 666, 982

Evans, N. J., Dunham, M. M., Jørgensen, J. K., Enoch, M. L., Merín, B., van Dishoeck, E. F., Alcalá, J. M., Myers, P. C., Stapelfeldt, K. R., Huard, T. L., Allen, L. E., Harvey, P. M., van Kempen, T., Blake, G. A., Koerner, D. W., Mundy, L. G., Padgett, D. L., & Sargent, A. I. 2009, ApJS, 181, 321

Fayolle, E. C., Öberg, K. I., Cuppen, H. M., Visser, R., & Linnartz, H. 2011, A&A, 529, A74

Flower, D. R., Pineau Des Forêts, G., & Walmsley, C. M. 2006, A&A, 449, 621

Friesen, R. K., Di Francesco, J., Myers, P. C., Belloche, A., Shirley, Y. L., Bourke, T. L., & André, P. 2010, ApJ, 718, 666

Froebrich, D. 2005, ApJS, 156, 169

Fuller, G. A., Lada, E. A., Masson, C. R., & Myers, P. C. 1995, ApJ, 453, 754

Fuller, G. A., & Wootten, A. 2000, ApJ, 534, 854

Goldsmith, P. F., & Langer, W. D. 1999, ApJ, 517, 209

Gueth, F., Bachiller, R., & Tafalla, M. 2003, A&A, 401, L5

Gueth, F., Guilloteau, S., & Bachiller, R. 1996, A&A, 307, 891

Gueth, F., Guilloteau, S., Dutrey, A., & Bachiller, R. 1997, A&A, 323, 943

Hartmann, L., Calvet, N., Allen, L., Chen, H., & Jayawardhana, R. 1999, AJ, 118, 1784

Herbig, G. H., & Jones, B. F. 1983, AJ, 88, 1040

Herbst, E. 1982, A&A, 111, 76

Hirota, T., Honma, M., Imai, H., Sunada, K., Ueno, Y., Kobayashi, H., & Kawaguchi, N. 2011, PASJ, 63, 1

Hogerheijde, M. R., & Sandell, G. 2000, ApJ, 534, 880

Hogerheijde, M. R., van Dishoeck, E. F., Blake, G. A., & van Langevelde, H. J. 1998, ApJ, 502, 315

Jørgensen, J. K. 2004, A&A, 424, 589

Jørgensen, J. K., Bourke, T. L., Myers, P. C., Di Francesco, J., van Dishoeck, E. F., Lee, C., Ohashi, N., Schöier, F. L., Takakuwa, S., Wilner, D. J., & Zhang, Q. 2007, ApJ, 659, 479

Kenyon, S. J., Hartmann, L. W., Strom, K. M., & Strom, S. E. 1990, AJ, 99, 869

Keto, E., & Rybicki, G. 2010, ApJ, 716, 1315

Kim, H. J., Evans, II, N. J., Dunham, M. M., Lee, J.-E., & Pontoppidan, K. M. 2012, ApJ, 758, 38

Kirk, J. M., Ward-Thompson, D., Di Francesco, J., Bourke, T. L., Evans, N. J., Merín, B., Allen, L. E., Cieza, L. A., Dunham, M. M., Harvey, P., Huard, T., Jørgensen, J. K., Miller, J. F., Noriega-Crespo, A., Peterson, D., Ray, T. P., & Rebull, L. M. 2009, ApJS, 185, 198

Langer, W. D. 1985, in Protostars and Planets II, ed. D. C. Black & M. S. Matthews, 650–667

Lee, C., Hirano, N., Palau, A., Ho, P. T. P., Bourke, T. L., Zhang, Q., & Shang, H. 2009, ApJ, 699, 1584

Lee, J., Bergin, E. A., & Evans, II, N. J. 2004, ApJ, 617, 360

Lee, J.-E. 2007, Journal of Korean Astronomical Society, 40, 83

Loinard, L., Torres, R. M., Mioduszewski, A. J., Rodríguez, L. F., González-Lópezlira, R. A., Lachaume, R., Vázquez, V., & González, E. 2007, ApJ, 671, 546

Looney, L. W., Tobin, J. J., & Kwon, W. 2007, ApJ, 670, L131

Lovas, F. J. 1992, Journal of Physical and Chemical Reference Data, 21, 181

Öberg, K. I., Boogert, A. C. A., Pontoppidan, K. M., van den Broek, S., van Dishoeck, E. F., Bottinelli, S., Blake, G. A., & Evans, II, N. J. 2011, ApJ, 740, 109

Pagani, L., Vastel, C., Hugo, E., Kokoouline, V., Greene, C. H., Bacmann, A., Bayet, E., Ceccarelli, C., Peng, R., & Schlemmer, S. 2009, A&A, 494, 623

Parise, B., Belloche, A., Du, F., Güsten, R., & Menten, K. M. 2011, A&A, 526, A31

Roberts, H., & Millar, T. J. 2000, A&A, 361, 388

—. 2007, A&A, 471, 849

Sault, R. J., Teuben, P. J., & Wright, M. C. H. 1995, in Astronomical Society of the Pacific Conference Series, Vol. 77, Astronomical Data Analysis Software and Systems IV, ed. R. A. Shaw, H. E. Payne, & J. J. E. Hayes, 433–+

Scholz, A., Wood, K., Wilner, D., Jayawardhana, R., Delorme, P., Caratti O Garatti, A., Ivanov, V. D., Saviane, I., & Whitney, B. 2010, MNRAS, 409, 1557

Shirley, Y. L., Evans, II, N. J., Rawlings, J. M. C., & Gregersen, E. M. 2000, ApJS, 131, 249

Shu, F. H. 1977, ApJ, 214, 488

Sipilä, O., Hugo, E., Harju, J., Asvany, O., Juvela, M., & Schlemmer, S. 2010, A&A, 509, A98

Terebey, S., Fich, M., Noriega-Crespo, A., Padgett, D. L., Fukagawa, M., Audard, M., Brooke, T., Carey, S., Evans, N. J., Guedel, M., Hines, D., Huard, T., Knapp, G. R., McCabe, C., Menard, F., Monin, J., & Rebull, L. 2009, ApJ, 696, 1918

Tobin, J. J., Hartmann, L., Bergin, E., Chiang, H.-F., Looney, L. W., Chandler, C. J., Maret, S., & Heitsch, F. 2012, ApJ, 748, 16

Tobin, J. J., Hartmann, L., Calvet, N., & D'Alessio, P. 2008, ApJ, 679, 1364

Tobin, J. J., Hartmann, L., Chiang, H.-F., Looney, L. W., Bergin, E. A., Chandler, C. J., Masqué, J. M., Maret, S., & Heitsch, F. 2011, ApJ, 740, 45

Tobin, J. J., Hartmann, L., Looney, L. W., & Chiang, H. 2010, ApJ, 712, 1010

Tsitali, A. E., Bourke, T. L., Peterson, D. E., Myers, P. C., Dunham, M. M., Evans, N. J., & Huard, T. L. 2010, ApJ, 725, 2461

Visser, A. E., Richer, J. S., & Chandler, C. J. 2002, AJ, 124, 2756

Visser, R., & Bergin, E. A. 2012, ApJ, 754, L18

Watson, W. D. 1974, ApJ, 188, 35

Young, C. H., & Evans, II, N. J. 2005, ApJ, 627, 293

Young, K. E., Enoch, M. L., Evans, II, N. J., Glenn, J., Sargent, A., Huard, T. L., Aguirre, J., Golwala, S., Haig, D., Harvey, P., Laurent, G., Mauskopf, P., & Sayers, J. 2006, ApJ, 644, 326

This preprint was prepared with the AAS LaTeX macros v5.2.

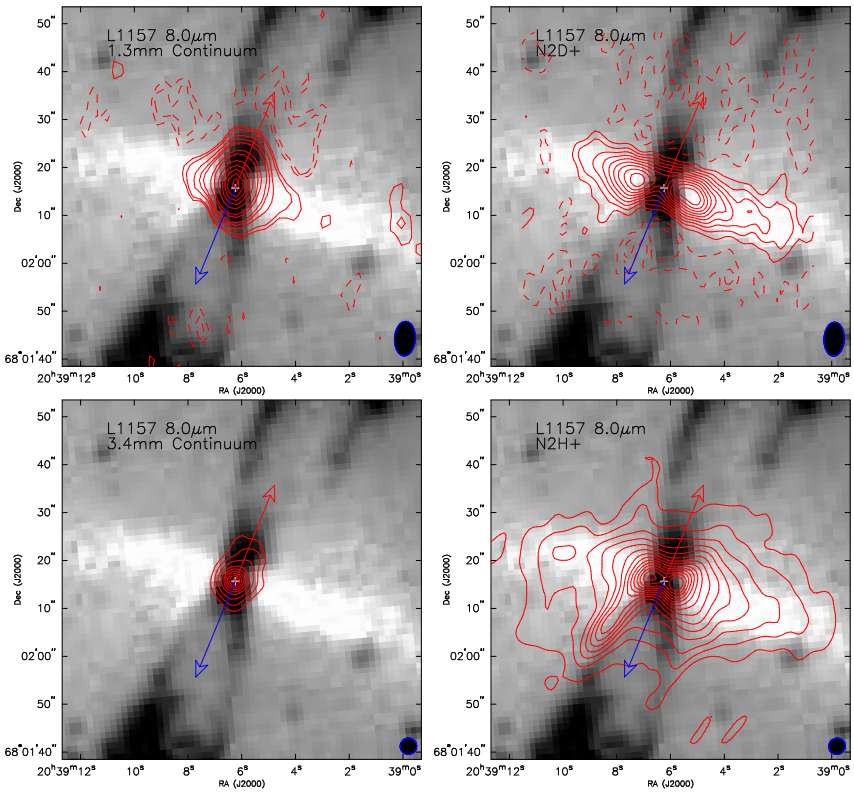

Fig. 1.— L1157– Data from the SMA and PdBI overlaid on the IRAC 8 μm image (inverse grayscale). The *top left panel* shows the SMA 1.3 mm continuum emission (contours) which peaks on the protostar but is also extended at low surface brightness levels along the envelope viewed in 8 μm extinction; contours are $\pm 2\sigma$, ± 3, 6, 9, 12, 22, 30, 50, ..., 150σ, where σ = 2.16 mJy beam^{-1}. The *top right panel* shows the SMA N_2D^+ ($J = 3 \rightarrow 2$) integrated intensity emission, the contours start at and increase in units of $\pm 3\sigma$, where σ = 0.07 K km s^{-1}. The N_2D^+ emission shows a local minimum on the protostar position and peaks at R $\sim$ 2000 AU. The *bottom left panel* shows the PdBI 3.4 mm continuum emission (contours) which peaks on the protostar; contours are $\pm 2\sigma$, ± 3, 6, 12, 24, 36, ..., 96σ, where σ = 0.24 mJy beam^{-1}. The *bottom right panel* show the PdBI + IRAM 30m N_2H^+ ($J = 1 \rightarrow 0$) integrated intensity emission; the contours start at and increase in units of $\pm 30\sigma$, where σ = 0.042 K km s^{-1}. The N_2H^+ emission also shows a local minimum at the location of the protostar, but the peak emission is located at R$\sim$1000 AU and inside the peak N_2D^+ emission. The SMA beam is 7.1″ × 4.3″ and the PdBI beam is 3.4″ × 3.3″.

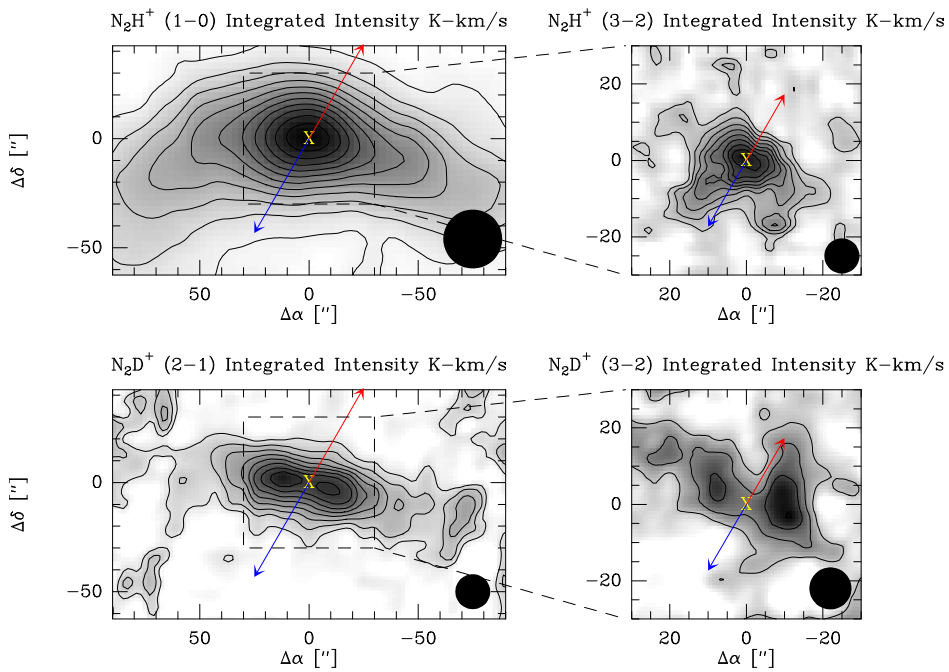

Fig. 2.— L1157– Single-dish mapping from the IRAM 30m. The *top panels* show the N_2H^+ ($J = 1 \rightarrow 0$) and ($J = 3 \rightarrow 2$) emission, respectively. The *bottom panels* show the N_2D^+ ($J = 2 \rightarrow 1$) and ($J = 3 \rightarrow 2$) emission. The N_2H^+ emission is centrally peaked and the N_2H^+ ($J = 3 \rightarrow 2$) appears elongated normal to the outflow, consistent with the double-peaked N_2H^+ ($J = 1 \rightarrow 0$) map from the PdBI (Figure 1). The N_2D^+ emission then appears double-peaked in both transitions, consistent with the SMA N_2D^+ observations. The contours and beam in each panel are drawn as follows: N_2H^+ ($J = 1 \rightarrow 0$) 10σ, 30σ, 50σ, ..., and σ=0.027 K km s^{-1}, 27″ beam; N_2H^+ ($J = 3 \rightarrow 2$) 4σ, 6σ, ..., and σ=0.14 K km s^{-1}, 9″ beam; N_2D^+ ($J = 2 \rightarrow 1$) 2σ, 4σ, ..., and σ=0.05 K km s^{-1}, 16″ beam; N_2D^+ ($J = 3 \rightarrow 2$) 2σ, 4σ, ..., and σ=0.12 K km s^{-1}, 11″ beam.

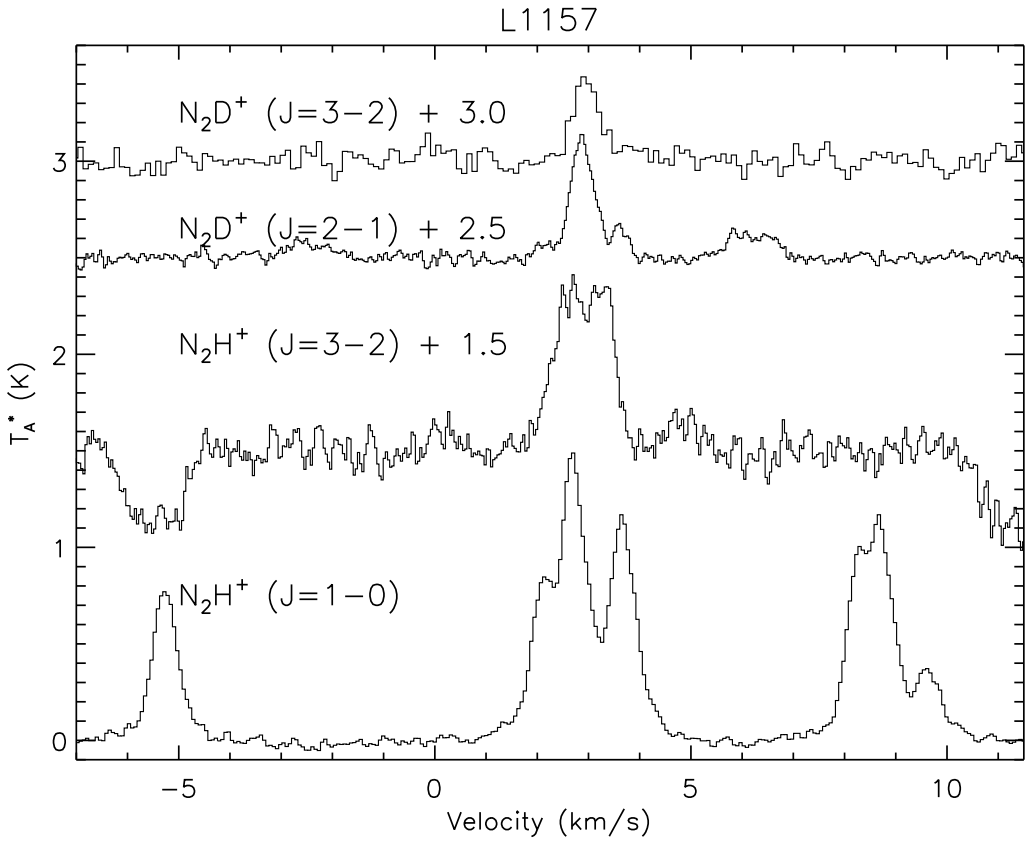

Fig. 3.— Example spectra of N_2H^+ and N_2D^+ taken toward L1157. The spectra are averaged over an aperture radius of 12″ centered on the protostar position. Faint hyperfine lines are visible in the N_2H^+ ($J = 3 \rightarrow 2$) at 0 and 5 km s^{-1} and in N_2D^+ ($J = 2 \rightarrow 1$) at -3 and 6 km s^{-1}. The signal-to-noise is too low to see hyperfine lines in N_2D^+ ($J = 3 \rightarrow 2$). The negative features in the N_2H^+ ($J = 3 \rightarrow 2$) at -5 and -12 km s^{-1} are frequency switching artifacts.

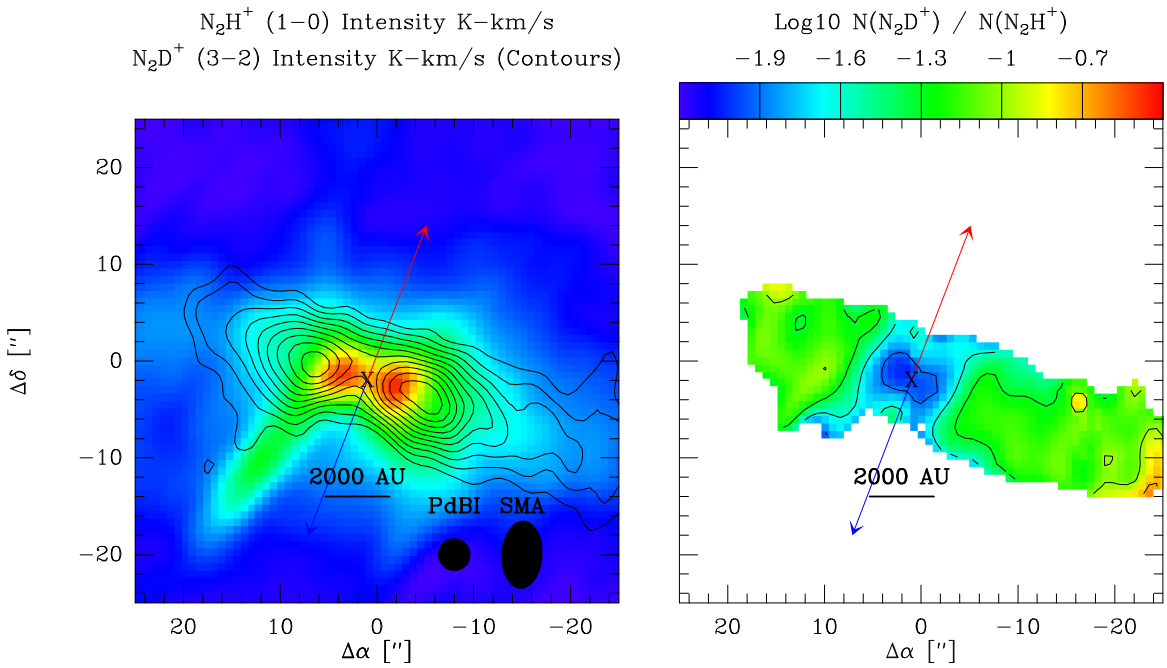

Fig. 4.— Comparison of N_2H^+ and N_2D^+ emission and column density ratio map. The *left panel* shows the N_2D^+ integrated intensity (contours) overlaid on the PdBI N_2H^+ integrated intensity (color scale). The *right panel* shows the column density ratio of N_2D^+ to N_2H^+. The color stretch in the left panel goes from 0 to 21 K km s^{-1} and the contours start 3σ and increase with this interval ($\sigma = 0.07$ K km s^{-1}).

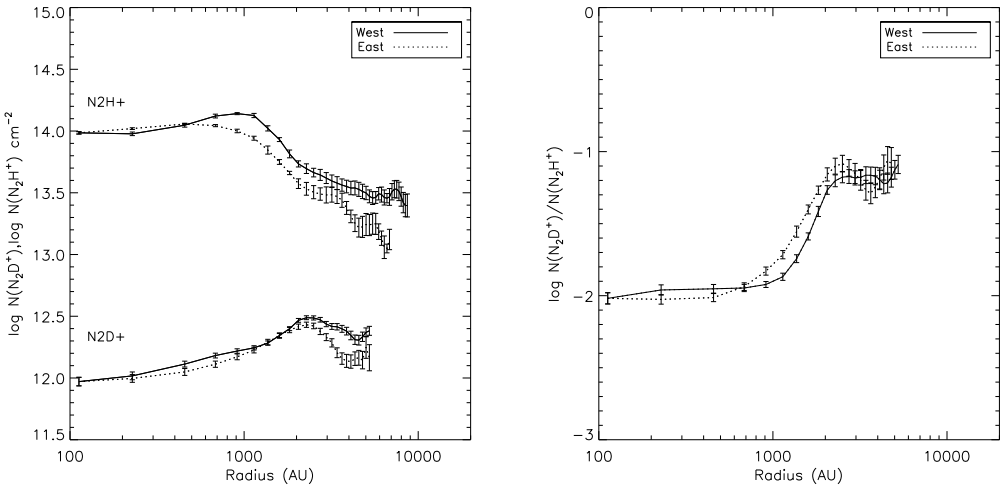

Fig. 5.— N_2H^+ and N_2D^+ column density and column density ratio plots. The *left panel* shows the column density of N_2H^+ and N_2D^+ derived from the integrated intensity maps. The right panel shows the N_2D^+/N_2H^+ column density ratio. Note the clear 1000 AU separation of N_2H^+ and N_2D^+ column density peaks. The error bars on the N_2H^+ data are the combination of noise, error in excitation temperature, and error in optical depth. The error bars on the N_2D^+ data only include noise since the emission is optically thin and we adopt the excitation temperature of the N_2H^+ data. The solid lines are taken from the west side of the envelope and the dotted lines are from the east side.

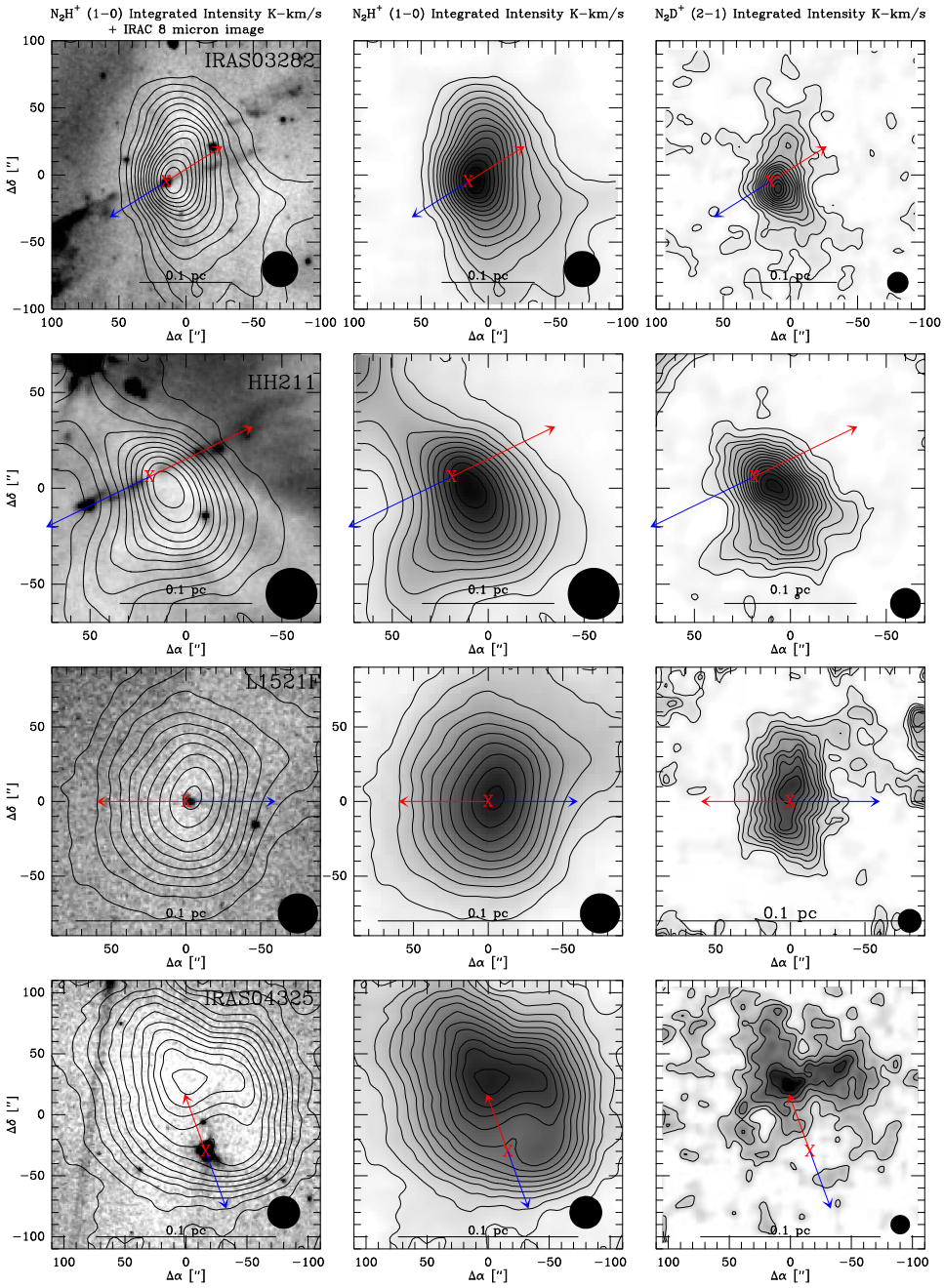

Fig. 6.— Single-dish integrated intensity maps of N_2H^+ ($J = 1 \rightarrow 0$) and N_2D^+ ($J = 2 \rightarrow 1$) for the protostars identified in each panel. The left panels show the N_2H^+ ($J = 1 \rightarrow 0$) emission overlaid on the IRAC 8 μm image, the middle panels show the N_2H^+ ($J = 1 \rightarrow 0$) as contours and grayscale, and the right panels show the N_2D^+ ($J = 2 \rightarrow 1$) emission as grayscale and contours. Eight of thirteen well-resolved sources show spatial differentiation between the N_2H^+ and N_2D^+ emission peaks; however, they are not as regular as in L1157. All N_2H^+ contours start at 10σ and increase by 10σ and all the N_2D^+ contours start at 3σ and increase in 3σ intervals; the values for σ are given in Table 3 for each source. The IRAM 30m beam for the N_2H^+ ($J = 1 \rightarrow 0$) data is $27''$ and $16''$ for the N_2D^+ ($J = 2 \rightarrow 1$) data.

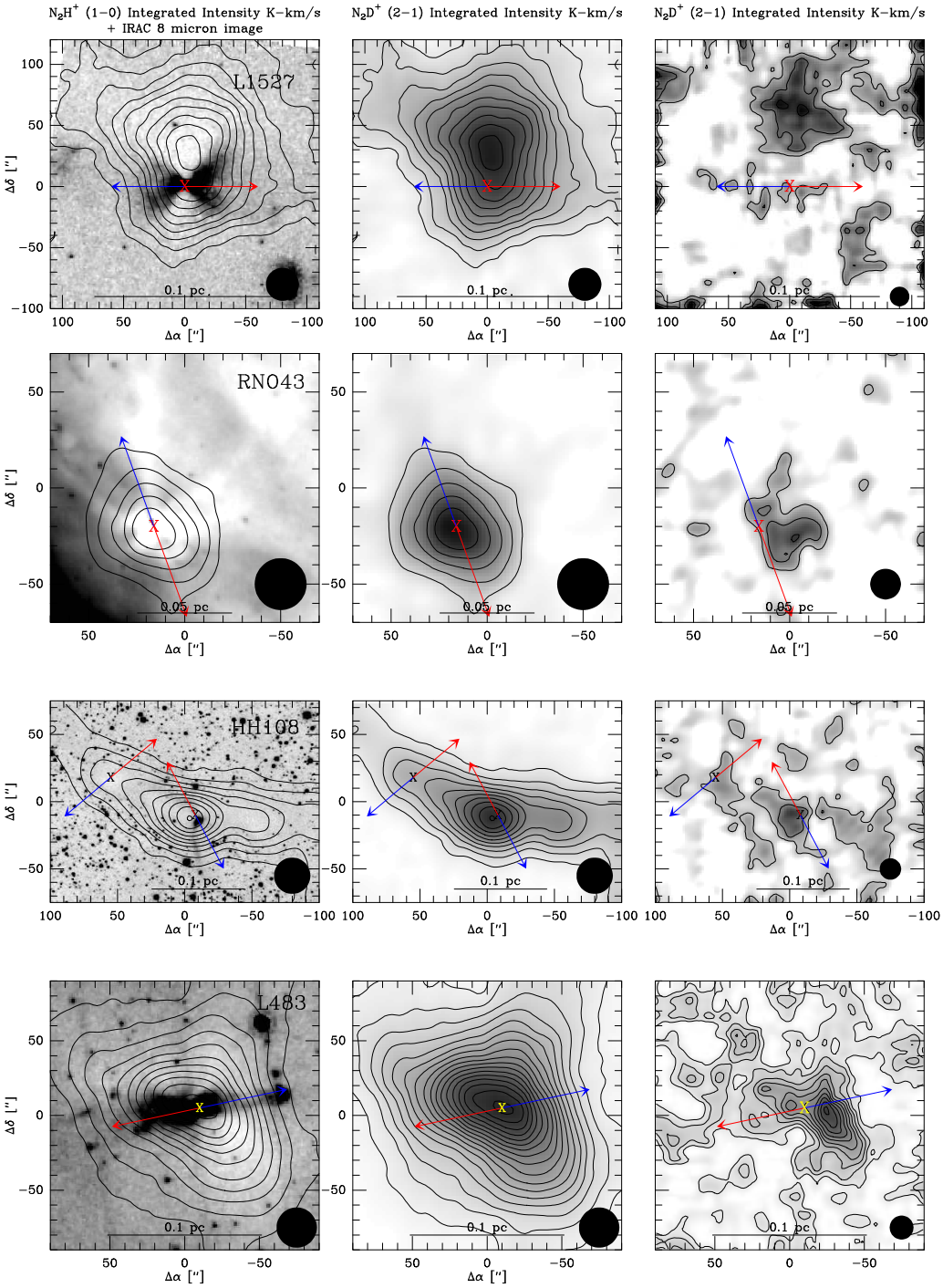
N2H+ (1−0) Integrated Intensity K−km/s
+ IRAC 8 micron image
N2D+ (2−1) Integrated Intensity K−km/s
N2D+ (2−1) Integrated Intensity K−km/s
L1527
RNO43
HH108
L483
0.1 pc
0.05 pc
Δα ["]
Δδ ["]

Fig. 6b.—

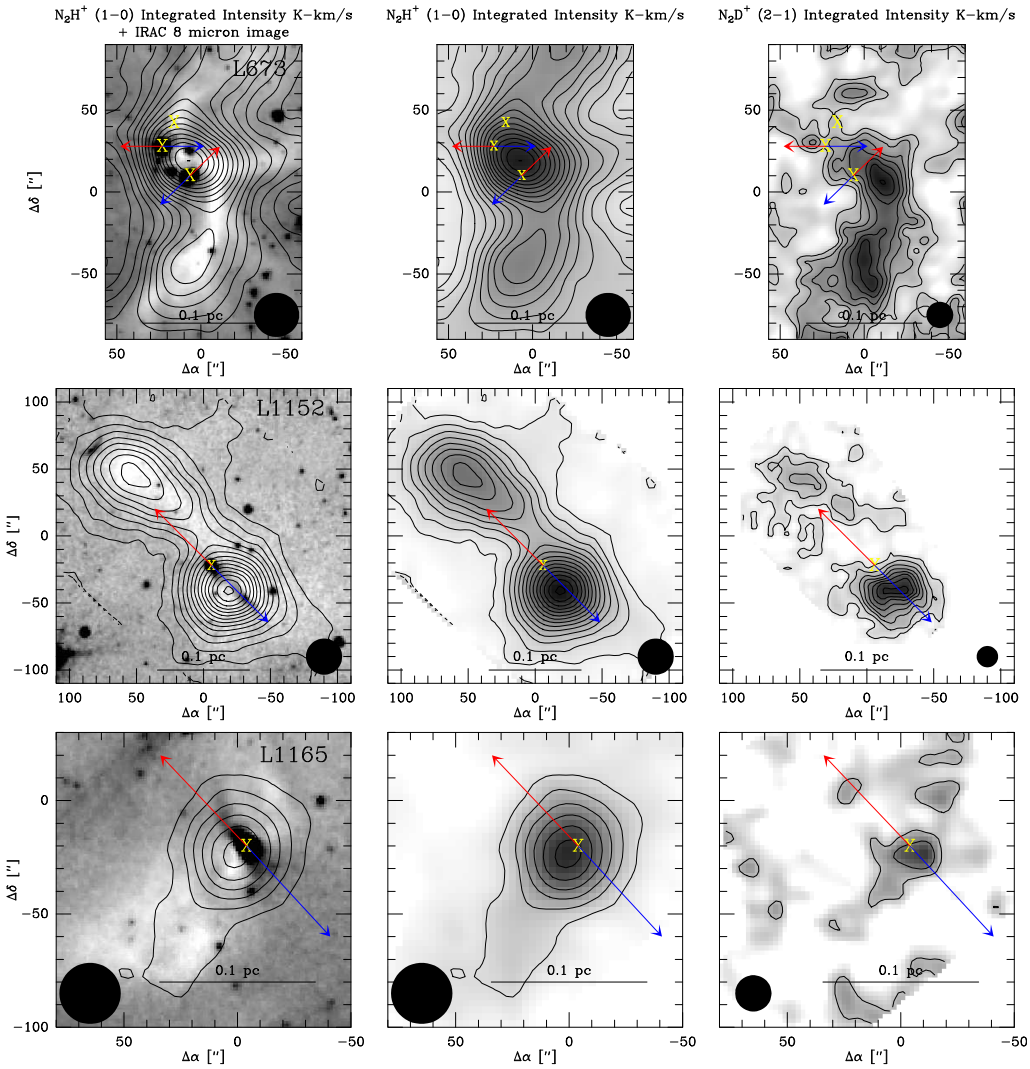
N2H+ (1−0) Integrated Intensity K−km/s
+ IRAC 8 micron image
N2H+ (1−0) Integrated Intensity K−km/s
N2D+ (2−1) Integrated Intensity K−km/s
L673
L1152
L1165
0.1 pc
Δα ["]
Δδ ["]

Fig. 6c.—

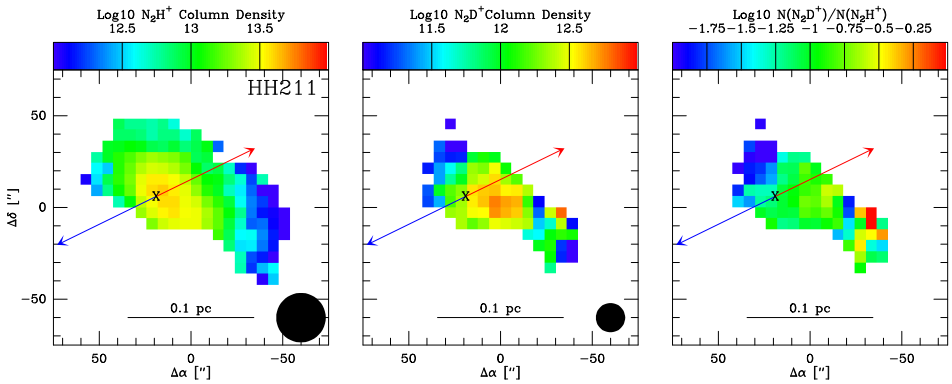

Fig. 7.— Spatial distribution of N_2H^+ column density (left panel), N_2D^+ (center panel), and their ratios (right panel) for HH211. Notice the column density peak of N_2H^+ at the location of the protostar, while the emission peak was offset in Figure 6.

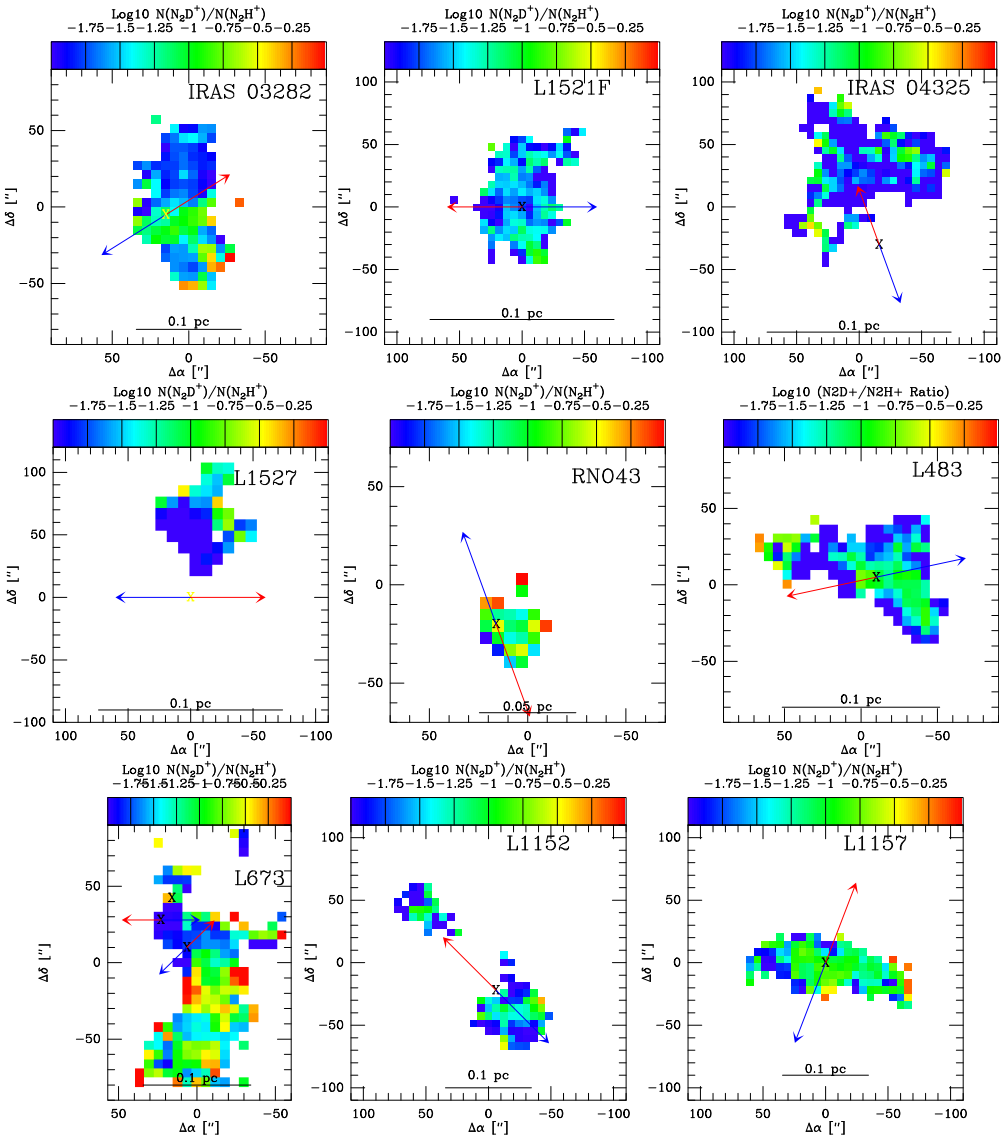

Fig. 8.— Column density ratio maps for all sources except HH211 (Figure 7), L1165, and HH108.

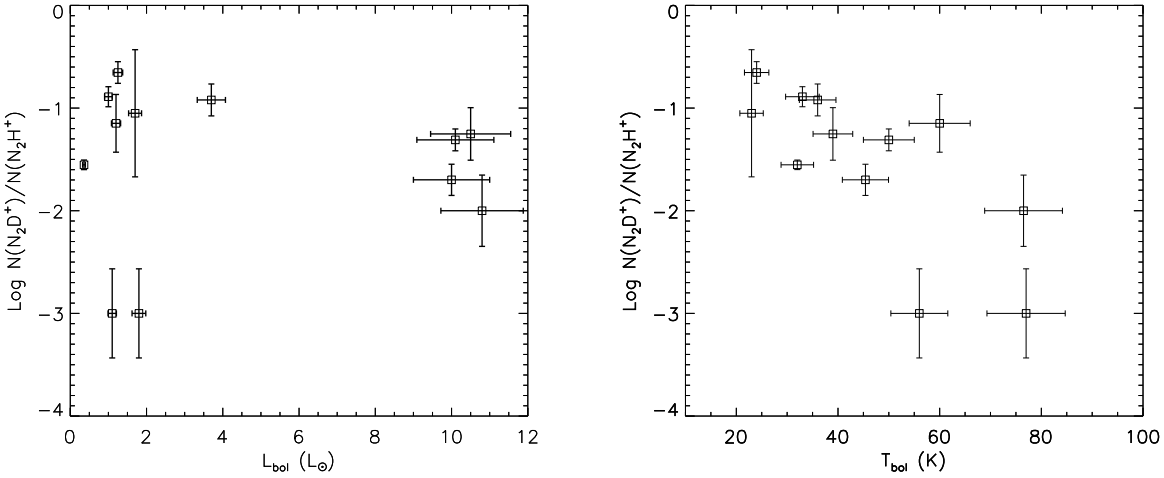

Fig. 9.— N_2D^+ to N_2H^+ ratio plotted versus bolometric luminosity (left panel) and bolometric temperature (right panel). Higher luminosity sources tend to have a lower N_2D^+/N_2H^+ ratio, while lower luminosity sources have a range of deuteration. There appears to be a trend in bolometric temperature versus N_2D^+/N_2H^+ ratio with deuteration decreasing with evolution, consistent with (Emprechtinger et al. 2009).

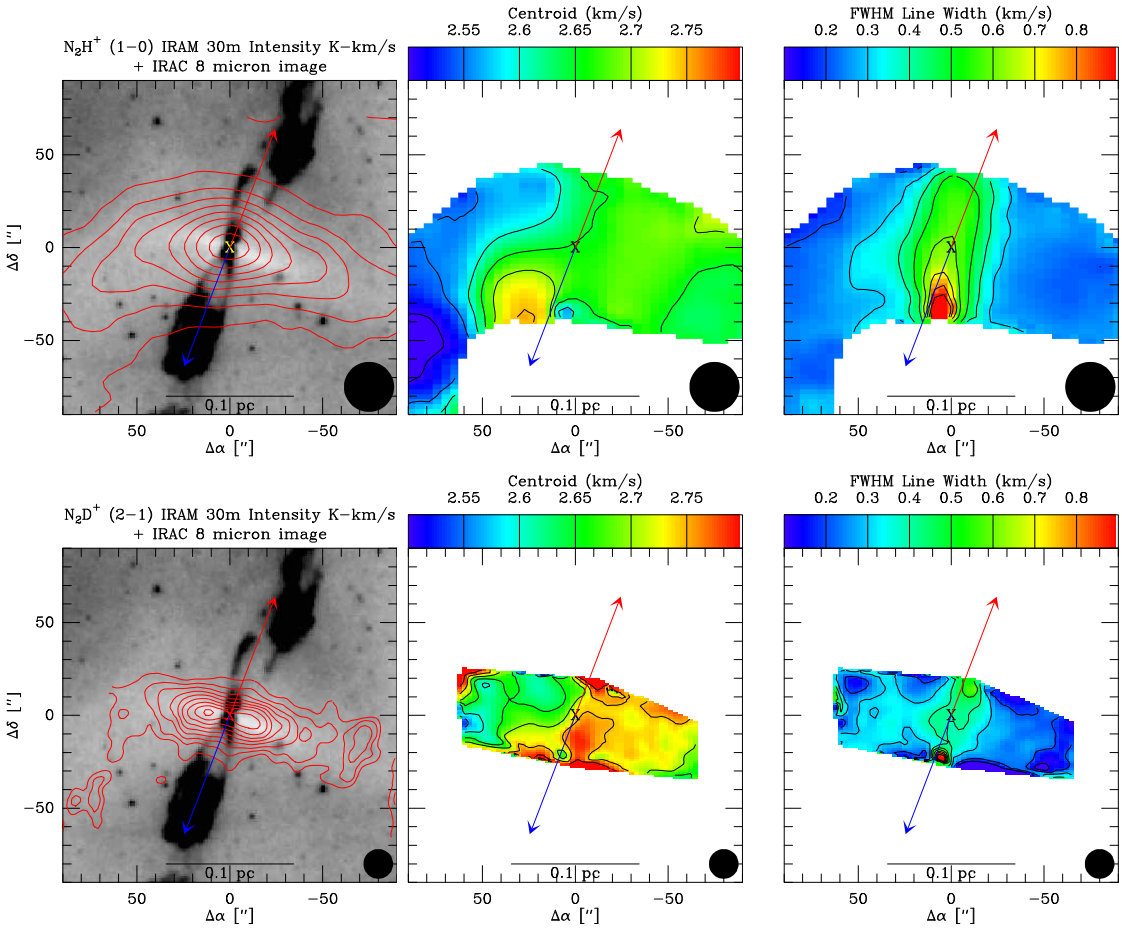

Fig. 10.— Kinematic comparison of N_2H^+ and N_2D^+ from the IRAM 30m data of L1157. The top row shows the IRAM 30m N_2H^+ ($J = 1 \rightarrow 0$) integrated intensity (*left panel*), line-center velocity (*middle panel*), and linewidth (*right panel*). The bottom row shows the same information as the top but for N_2D^+ ($J = 2 \rightarrow 1$). The line-center velocities for N_2D^+ are about 0.1 km s^{-1} more redshifted on the west side of the envelope than on the east side and the linewidths of N_2D^+ are lower than the N_2H^+ linewidths toward the protostar.

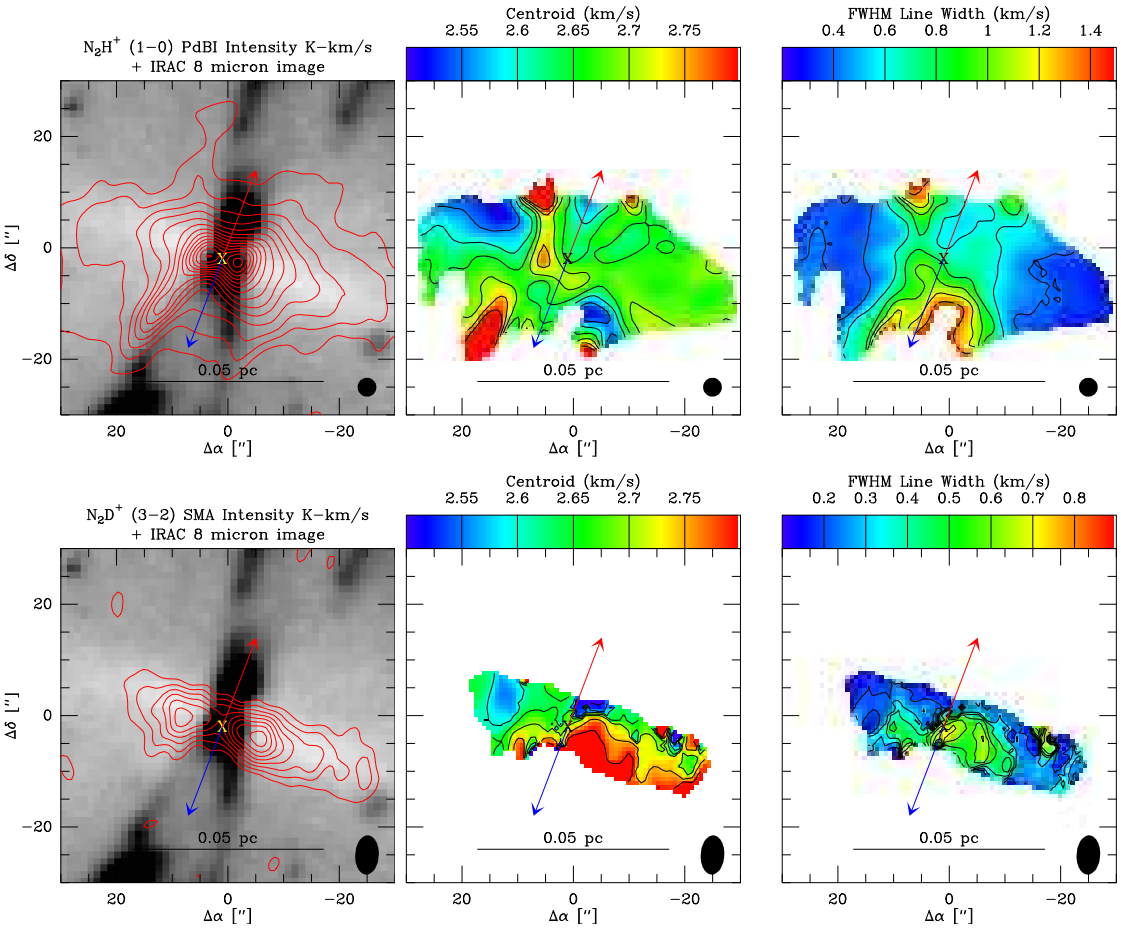

Fig. 11.— Kinematic comparison of interferometric N_2H^+ and N_2D^+ data of L1157. The top row shows the PdBI N_2H^+ ($J = 1 \rightarrow 0$) integrated intensity (*left panel*), line-center velocity (*middle panel*), and linewidth (*right panel*). The bottom row shows the same information as the top but for SMA N_2D^+ ($J = 3 \rightarrow 2$). The velocity structure of N_2H^+ in the line-center velocities and linewidth is much more complex than N_2D^+ due to the outflow interaction with the envelope (Tobin et al. 2011). The more redshifted gas on the west side of the envelope also appears in the N_2D^+ ($J = 3 \rightarrow 2$) which is also present in the single-dish N_2D^+.

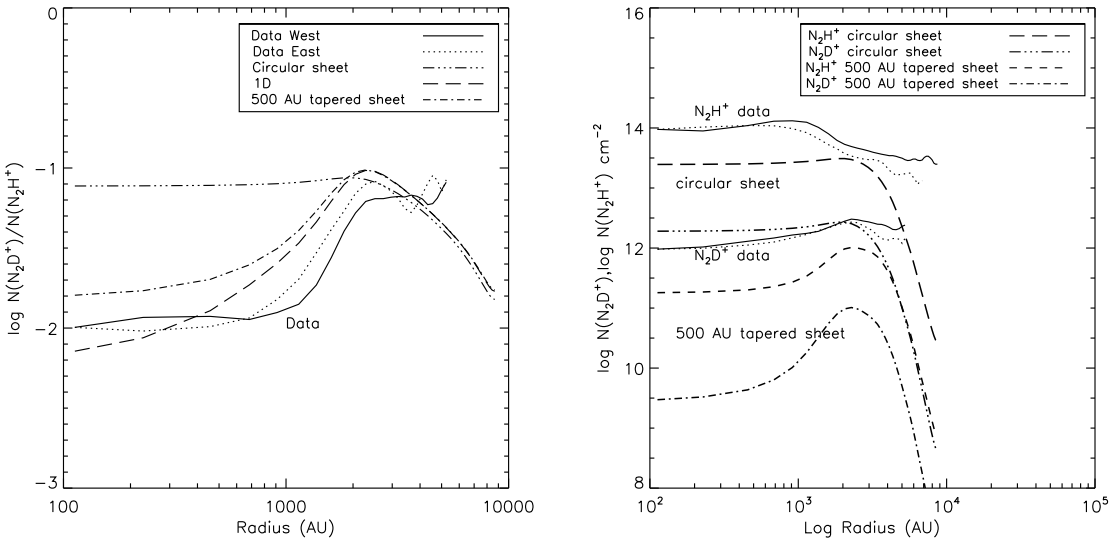

Fig. 12.— Abundance ratio and integrated column densities of N_2H^+ and N_2D^+ compared to models. The abundance ratio of the 1D model and tapered sheet (filament) resemble the abundance ratio of the data; however, the absolute column densities do not match the data. The *left* panel shows the abundance ratio of N_2D^+ to N_2H^+ from the 1D chemical model calculation (dashed-line), integrated through a circular sheet with a radius of 15000 AU (triple dot-dashed line) and an approximated filamentary envelope, produced by tapering the circular sheet by a Gaussian with $\sigma = 500$ AU (single dot-dashed line). The data are shown as the solid and dotted lines from the east and west sides of the envelope respectively. The *right* panel shows the column density of N_2H^+ and N_2D^+ derived from integrated maps, assuming that N_2D^+ has the same excitation temperature as N_2H^+. The data are shown as the solid and dotted lines from the east and west sides of the envelope respectively and the model data are shown as the dashed or dot-dashed lines. Note the coincidence of column density peaks in the models for N_2D^+; moreover, the peaks are most apparent in the filament model rather than the sheet.

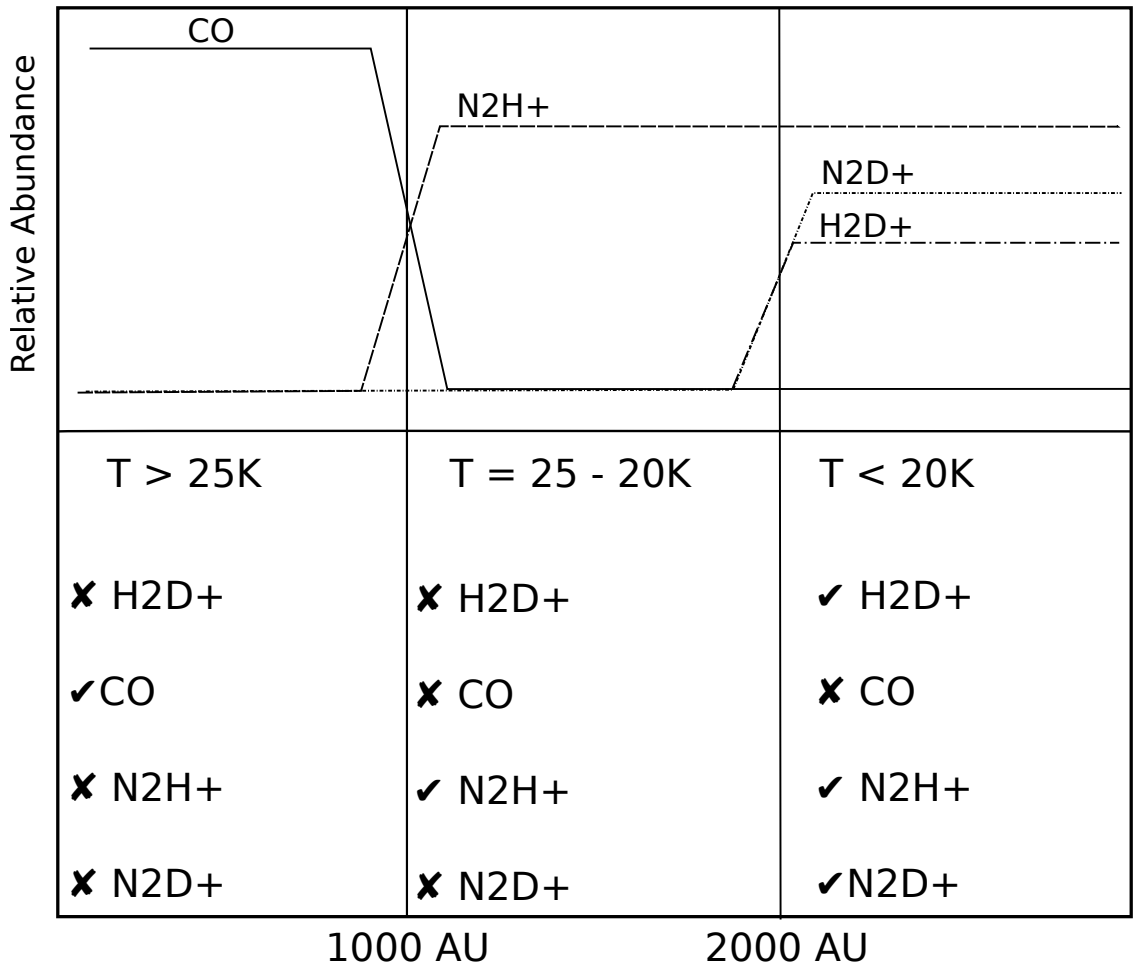

Fig. 13.— Schematic diagram for spatial distribution of N_2H^+ and N_2D^+ in L1157. The upper panel shows the suggested relative abundances of each species as a function of radius and temperature and the bottom panel identifies the temperature range and which species are present in the gas phase for the case of increased CO evaporation temperature. Inside of 1000 AU, CO is in the gas phase, evaporated off the dust grains, and destroys the N_2H^+. At radii between 1000 AU and 2000 AU the CO may remain frozen on the dust grains at the expected temperatures of 20 to 25 K; this enables N_2H^+ to be abundant, but H_2D^+ is destroyed due to the back reaction operating (Equation 1) at these temperatures, keeping N_2D^+ abundances low. At radii greater than 2000 AU, the temperature is below 20 K and H_2D^+ will be present, enabling N_2D^+ to form and have its abundance peaks at this radius. If there is an H_2 OPR gradient rather than an increased CO evaporation temperature, N_2D^+ and H_2D^+ may only be present at $T < 15$ K and CO could then evaporate at $T > 20$ K and still show the same abundance offset.

Table 1. Source Properties

Source	RA (J2000)	Dec (J2000)	Distance (pc)	$Mass_{8\mu m}$ ($M_\odot$) (r<0.05pc)	$Mass_{submm}$* ($M_\odot$)	L_{bol} ($L_\odot$)	T_{bol} (K)	Outflow PA (°)	References (Distance, M_{ref}, L_{bol},) (T_{bol}, Outflow PA)
IRAS 03282+3035	03:31:21.10	+30:45:30.2	230	2.4	2.2	1.2	33	122	23, 4, 3, 3, 26
HH211	03:43:56.78	+32:00:49.8	230	1.1	1.5	3.02	24	116	23, 3, 3, 3, 6
L1521F	04:28:39.03	+26:51:35.0	140	2.3	1.0	0.35	∼20	270	20, 10, 8, 1, 7
IRAS 04325+2402	04:35:35.39	+24:08:19.0	140	3.9	-	0.97	73	200	20, 1, 15, 15, 16
L1527	04:39:53.86	+26:03:09.5	140	0.8	2.4	1.9	56	90	20, 4, 9, 15, 31
RNO43	05:32:19.39	+12:49:40.8	460	2.8	2.6	12.5	56	20	21, 10, 2, 15, 21 & 1
L483	18:17:29.93	-04:39:39.6	200	3.5	1.8	11.5	<54	282	25, 4, 3, 15, 30
HH108 IRS	18:35:42.14	-00:33:18.5	300	-	4.5	∼8.0	28	208	17, 14, 14, 1, 1
HH108 MMS	18:35:46.46	-00:32:51.2	300	-	3.6	0.7	18	130	17, 17, 1, 1, 1
L673-SMM2	19:20:25.96	+11:19:52.9	300	1.0	0.35	2.8	-	270, 135	24, -, -, 12, 1 & 12
L1152	20:35:46.22	+67:53:01.9	300	3.4	12.0	1.0	33	225	5, 10, 3, 1, 11
L1157	20:39:06.25	+68:02:15.9	300	2.6	2.2	3.0	29	150	5, 4, 3, 15, 27
L1165	22:06:50.46	+59:02:45.9	300	1.1	0.32	13.9	46	225	5, 1, 12, 1, 12

Note. — Properties of sources observed in the single-dish and/or interferometric sample. The 8μm extinction masses are taken within 0.05 pc of the protostar and note that some of the masses have been rescaled to account for a different distance estimate as compared to Paper I. Positions are reflect the coordinates of the 24μm point source from *Spitzer* data or the 3mm continuum continuum position for protostars observed with CARMA. The Outflow position axes (PA) are not well constrained since the outflows are known to precess they can have fairly large angular width; a conservative estimate of uncertainty would be ±10°. References: (1) This work, (2) Tobin et al. (2010), (3) Enoch et al. (2009), (4) Shirley et al. (2000), (5) Kirk et al. (2009), (6) Lee et al. (2009), (7) Bourke et al. (2006) (8) Terebey et al. (2009), (9) Tobin et al. (2008), (10) Young et al. (2006), (3) Visser et al. (2002), (11) Chapman & Mundy (2009), (14) Enoch et al. (2007), (15) Froebrich (2005), (16) Hartmann et al. (1999), (17) Chini et al. (2001), (20) Loinard et al. (2007), (21) Bence et al. (1996), (23) Hirota et al. (2011), (24) Herbig & Jones (1983), (25) Jørgensen (2004), (26) Arce & Sargent (2006), (27) Gueth et al. (1996), (30) Fuller et al. (1995), (31) Hogerheijde et al. (1998).

*Mass computed from sub/millimeter emission assuming an isothermal temperature.

Table 2. Observed Species

Transition	Frequency (GHz)	Observatory	Beam width (″)	F_{eff}	B_{eff}
N_2H^+ ($J = 1 \rightarrow 0$)	93.1737637	IRAM 30m	26	0.95	0.81
		PdBI D, C-array	3.4 x 3.3		
N_2H^+ ($J = 3 \rightarrow 2$)	279.511832	IRAM 30m	9	0.88	0.53
N_2D^+ ($J = 2 \rightarrow 1$)	154.217206	IRAM 30m	16	0.93	0.74
N_2D^+ ($J = 3 \rightarrow 2$)	231.321966	IRAM 30m	10	0.94	0.63
		SMA sub-compact	7.1 x 4.3		

Note. — The single-dish data were rescaled to main beam brightness temperatures (T_{mb}) where $T_{mb} = F_{eff}T_A^*/B_{eff}$. F_{eff} is the forward efficiency, accounting for losses by the secondary support structure, and B_{eff} is the main beam efficiency, the ratio of the main beam solid angle over the entire antenna pattern (http://www.iram.es/IRAMES/mainWiki/Iram30mEfficiencies).

Table 3. IRAM 30m Observations

Source	RA (J2000)	Dec (J2000)	Date (UT)	T_{sys}† (K)	Channel Width† (kHz)	σ_I† (K km s^{-1})
IRAS 03282+3035	03:31:19.8	+30:45:37	25 Oct 2009	115, 130	20, 40	0.04, 0.035
HH211-mm	03:43:55.3	+32:00:46	24 Oct 2009	110, 120	20, 40	0.05, 0.04
L1521F	04:28:39.0	+26:51:37	24 Oct 2009	102, 110	20, 40	0.04, 0.025
IRAS04325+2402	04:35:36.6	+24:08:54	25 Oct 2009	105, 120	20, 40	0.04, 0.035
L1527	04:39:54.0	+26:03:22	26 Oct 2009	100, 130	20, 40	0.03, 0.015
RNO43	05:32:18.2	+12:50:01	24 Oct 2009	115, 135	20, 40	0.04, 0.03
L483	18:17:30.3	-04:39:40.6	25 Oct 2009	135, 180	20, 40	0.06, 0.05
HH108	18:35:42.7	-00:33:07	23 Oct 2009	140, 230	20, 40	0.05, 0.06
L673-SMM2	19:20:25.4	+11:19:44	23/24 Oct 2009	140, 210	20, 40	0.04, 0.04
L1152	20:35:47.17	+67:53:22	24 Oct 2009	120, 150	20, 40	0.04, 0.035
L1157	20:39:05.6	+68:02:13.2	25 Oct 2009	110, 115, 320, 290	20, 20, 40, 40	0.027, 0.05, 0.12, 0.14
L1165	22:06:50.8	+59:03:06.5	25 Oct 2009	110, 120	20, 40	0.04, 0.035

Note. — Observations of protostellar envelopes taken with the IRAM 30m telescope. The positions reflect the map center and not necessarily the protostar position.

†System temperatures, channel widths, and intensity uncertainties are given for 93 GHz and 154 GHz respectively. For L1157, values for 231 GHz and 279 GHz are also given.

Table 4. N_2H^+ and N_2D^+ Line Parameters

Source	W	V_{lsr}	ΔV	T_{ex}	τ	W	V_{lsr}	ΔV	T_{ex}	τ
	N_2H^+ $(J = 1 \rightarrow 0)$					N_2D^+ $(J = 2 \rightarrow 1)$				
	(K km s^{-1})	(km s^{-1})	(km s^{-1})	(K)	(nepers)	(K km s^{-1})	(km s^{-1})	(km s^{-1})	(K)	(nepers)
IRAS03282	6.37 ± 0.04	6.94 ± 0.003	0.40 ± 0.006	6.0 ± 0.6	4.8 ± 0.5	1.40 ± 0.04	7.01 ± 0.01	0.35 ± 0.02	4.2 ± 0.6	2.7 ± 0.6
HH211	5.90 ± 0.05	9.10 ± 0.003	0.45 ± 0.008	4.8 ± 0.5	6.9 ± 0.6	2.27 ± 0.05	9.18 ± 0.01	0.38 ± 0.03	4.3 ± 0.6	3.9 ± 0.8
L1521F	5.30 ± 0.02	6.47 ± 0.001	0.30 ± 0.001	4.5 ± 0.1	16.9 ± 0.2	0.93 ± 0.03	6.56 ± 0.01	0.27 ± 0.02	4.1 ± 0.2	2.2 ± 0.3
IRAS04325	4.31 ± 0.05	5.70 ± 0.004	0.39 ± 0.011	5.3 ± 1.1	4.1 ± 0.8	0.03 ± 0.02	5.66 ± 0.07	0.40 ± 0.11	4.7 ± 1.7	0.1 ± 0.0
IRAS04325N	6.40 ± 0.03	5.87 ± 0.003	0.33 ± 0.008	6.7 ± 1.1	4.9 ± 0.8	0.81 ± 0.03	5.94 ± 0.01	0.29 ± 0.02	21.7 ± 3.6	0.1 ± 0.0
L1527	3.24 ± 0.03	5.90 ± 0.004	0.33 ± 0.009	4.5 ± 0.8	5.9 ± 0.9	< 0.01	...	...	...	...
L1527N	2.87 ± 0.03	5.82 ± 0.004	0.32 ± 0.009	4.2 ± 0.7	6.6 ± 1.0	0.22 ± 0.01	5.81 ± 0.03	0.39 ± 0.08	6.4 ± 1.5	0.1 ± 0.0
RNO43	2.50 ± 0.03	10.25 ± 0.007	0.82 ± 0.019	5.5 ± 2.6	0.9 ± 0.4	0.30 ± 0.02	10.40 ± 0.04	0.69 ± 0.08	6.2 ± 3.0	0.1 ± 0.0
L483	12.03 ± 0.06	5.35 ± 0.006	0.42 ± 0.011	5.7 ± 0.2	13.7 ± 0.4	0.99 ± 0.07	5.39 ± 0.01	0.27 ± 0.02	3.4 ± 0.5	5.5 ± 1.2
HH108 IRS	5.47 ± 0.06	10.80 ± 0.008	0.55 ± 0.017	5.0 ± 1.1	4.4 ± 0.9	0.61 ± 0.04	10.78 ± 0.03	0.51 ± 0.08	10.1 ± 2.5	0.1 ± 0.0
HH108 MMS	2.12 ± 0.04	10.92 ± 0.005	0.38 ± 0.013	4.4 ± 1.4	3.3 ± 1.0	0.54 ± 0.05	10.95 ± 0.04	0.50 ± 0.10	4.7 ± 2.7	0.4 ± 2.8
L673S	7.30 ± 0.05	6.85 ± 0.006	0.55 ± 0.015	7.6 ± 2.1	2.6 ± 0.7	0.74 ± 0.03	6.84 ± 0.02	0.58 ± 0.06	10.6 ± 3.0	0.1 ± 0.0
L673M	6.63 ± 0.05	6.90 ± 0.008	0.68 ± 0.020	6.1 ± 1.4	2.9 ± 0.7	0.47 ± 0.04	6.93 ± 0.04	0.62 ± 0.08	7.7 ± 2.0	0.1 ± 0.0
L673N	5.37 ± 0.05	6.91 ± 0.009	0.70 ± 0.022	5.1 ± 1.1	3.4 ± 0.7	0.33 ± 0.03	6.90 ± 0.04	0.47 ± 0.12	3.8 ± 2.2	0.4 ± 3.3
L1152	4.17 ± 0.04	2.64 ± 0.005	0.40 ± 0.012	4.6 ± 0.9	6.0 ± 1.0	0.31 ± 0.03	2.71 ± 0.03	0.40 ± 0.07	3.0 ± 1.1	2.6 ± 1.8
L1157	4.85 ± 0.02	2.65 ± 0.007	0.57 ± 0.017	4.6 ± 0.9	4.5 ± 0.8	0.78 ± 0.05	2.73 ± 0.01	0.40 ± 0.02	3.6 ± 0.7	2.2 ± 0.5
L1165	1.50 ± 0.04	-1.61 ± 0.006	0.43 ± 0.015	3.9 ± 1.4	2.8 ± 1.0	0.04 ± 0.01	-1.61 ± 0.04	0.26 ± 0.09	5.7 ± 2.7	0.1 ± 0.0

Note. — The N_2H^+ and N_2D^+ integrated intensities are on the T_{mb} scale and do not include the ∼10% calibration error. Note that for N_2D^+ T_{ex} is not well constrained when $\tau < 0.1$ and the uncertainties for $\tau = 0.1$ are not meaningful.

Table 5. Column densities of $N_2H^+$and N_2D^+ Ratios and Offsets

Source	$N(N_2H^+)$ (cm^{-2})	$N(N_2D^+)$ (cm^{-2})	$N(N_2D^+)/N(N_2H^+)$	N2H+/N2D+ offset ($''$)
IRAS03282	$2.66 \times 10^{13} \pm 3.25 \times 10^{12}$	$3.42 \times 10^{12} \pm 6.52 \times 10^{11}$	0.129 ± 0.029	8
HH211	$3.41 \times 10^{13} \pm 4.17 \times 10^{12}$	$7.57 \times 10^{12} \pm 1.58 \times 10^{12}$	0.222 ± 0.054	20[†]
L1521F	$7.42 \times 10^{13} \pm 1.72 \times 10^{12}$	$2.09 \times 10^{12} \pm 2.00 \times 10^{11}$	0.028 ± 0.003	0
IRAS04325	$1.51 \times 10^{13} \pm 3.97 \times 10^{12}$	$< 1.6 \times 10^{10}$	< 0.001	...
IRAS04325N	$2.83 \times 10^{13} \pm 5.42 \times 10^{12}$	$4.05 \times 10^{11} \pm 4.89 \times 10^{10}$	0.014 ± 0.003	0
L1527	$1.59 \times 10^{13} \pm 3.53 \times 10^{12}$	$< 1.6 \times 10^{10}$	< 0.001	35
L1527N	$1.56 \times 10^{13} \pm 3.78 \times 10^{12}$	$1.85 \times 10^{11} \pm 3.59 \times 10^{10}$	0.012 ± 0.004	...
RNO43	$3.18 \times 10^{12} \pm 1.35 \times 10^{12}$	$1.79 \times 10^{11} \pm 7.02 \times 10^{10}$	0.056 ± 0.033	16
L483	$1.40 \times 10^{14} \pm 6.17 \times 10^{12}$	$6.92 \times 10^{12} \pm 1.60 \times 10^{12}$	0.049 ± 0.012	16
HH108 IRS	$2.01 \times 10^{13} \pm 5.41 \times 10^{12}$	$4.03 \times 10^{11} \pm 8.27 \times 10^{10}$	0.020 ± 0.007	0[a]
HH108 MMS	$5.99 \times 10^{12} \pm 2.55 \times 10^{12}$	$5.32 \times 10^{11} \pm 7.23 \times 10^{11}$	0.089 ± 0.127	...
L673S	$1.89 \times 10^{13} \pm 5.05 \times 10^{12}$	$3.47 \times 10^{11} \pm 5.89 \times 10^{10}$	0.018 ± 0.006	18
L673M	$1.77 \times 10^{13} \pm 4.56 \times 10^{12}$	$2.54 \times 10^{11} \pm 4.84 \times 10^{10}$	0.014 ± 0.005	...
L673N	$1.57 \times 10^{13} \pm 4.05 \times 10^{12}$	$2.60 \times 10^{11} \pm 3.98 \times 10^{11}$	0.017 ± 0.026	...
L1152	$2.09 \times 10^{13} \pm 5.20 \times 10^{12}$	$1.49 \times 10^{12} \pm 8.79 \times 10^{11}$	0.071 ± 0.046	0
L1157	$1.82 \times 10^{13} \pm 4.49 \times 10^{12}$	$2.19 \times 10^{12} \pm 5.58 \times 10^{11}$	0.120 ± 0.043	3.5
L1165	$3.76 \times 10^{12} \pm 1.97 \times 10^{12}$	$3.75 \times 10^{10} \pm 2.03 \times 10^{10}$	0.010 ± 0.008	8

[†]Taken from the column density maps, emission maps are spatially coincident.

[a]Shift between protostar and N_2H^+ is observed even though N_2H^+ and N_2D^+ are spatially coincident.